LAWRENCE
LIVERMORE
NATIONAL
LABORATORY

LLNL-JRNL-753091

Optimal Design of Fiber Reinforced Composite Structures and Their Direct Ink Write Fabrication

F. Fernandez, W. S. Compel, J. P. Lewicki, D. A. Tortorelli

June 14, 2018

Computer Methods in Applied Mechanics and Engineering 353, 277-307, 2019

Disclaimer

This document was prepared as an account of work sponsored by an agency of the United States government. Neither the United States government nor Lawrence Livermore National Security, LLC, nor any of their employees makes any warranty, expressed or implied, or assumes any legal liability or responsibility for the accuracy, completeness, or usefulness of any information, apparatus, product, or process disclosed, or represents that its use would not infringe privately owned rights. Reference herein to any specific commercial product, process, or service by trade name, trademark, manufacturer, or otherwise does not necessarily constitute or imply its endorsement, recommendation, or favoring by the United States government or Lawrence Livermore National Security, LLC. The views and opinions of authors expressed herein do not necessarily state or reflect those of the United States government or Lawrence Livermore National Security, LLC, and shall not be used for advertising or product endorsement purposes.

Optimal Design of Fiber Reinforced Composite Structures and Their Direct Ink Write Fabrication

LLNL-JRNL-753091

Felipe Fernandez*[1], W. Scott Compel[2], James P. Lewicki[2] and Daniel A. Tortorelli[1,2] 1
University of Illinois at Urbana-Champaign, IL, USA
[2] Lawrence Livermore National Laboratory, CA, USA, fernandezaya1@llnl.gov

2019

Abstract

The majority of the current structural optimization software does not accommodate manufacturing constraints. Therefore, substantial modifications are imposed upon optimized designs to make them manufacturable and hence nonoptimal. We propose to optimize the design of composite structures that are amenable to Additive Manufacturing (AM). The printing process chosen in our study is based on Direct Ink Writing (DIW) in which short carbon fibers in a thermoset resin are extruded through a moving nozzle to build up a structure. Since the fibers are primarily aligned in the flow direction of the extrudate, the DIW printing trajectory influences the material properties of the composite structure. To accommodate this, the extrudate trajectory follows the contours of parameterized level-set functions. The parametrization allows us to prescribe the material properties and impose many DIW manufacturing constraints such as no-overlap, no-sag, minimum radius of curvature and continuity of the toolpaths. Ultimately, we obtain optimal manufacturable toolpaths that start and finish at a boundary. To minimize the fabrication time, we formulate the linking sequence of the toolpaths as a traveling salesman problem which we solve to obtain the shortest continuous toolpath per layer. Several examples illustrate the optimization procedure. Validation is also performed.

1 Introduction

Composite materials are integral in the design of countless structures due to their favorable physical properties. Indeed, the mechanical properties of these materials are designed to be superior to those of their individual constituent materials. This is accomplished by optimally placing the constituents within the composite so as to tailor the material properties [1, 2]. Additive Manufacturing (AM) technology adds the potential for further control of this placement by depositing materials in precise microstructure patterns.

Structural optimization of laminated composite structures has been studied extensively. Problems have been solved to find optimal shape, thickness, number of plies, and/or stacking sequence of the laminates to maximize stiffness, failure load, etc. These challenging design problems are often nonlinear, non-convex, multi-modal, multi-dimensional and expressed with discrete and/or continuous design variables. To solve these problems, researchers have used gradient-based, direct search, heuristic, and hybrid optimization techniques. In general, gradient-based methods are the most efficient although they may only find local minima [3]. For more comprehensive reviews on the design of composite structures, the reader is referred to [4, 5, 1, 3].

Unfortunately, many optimized composite structures are not practical because current structural optimization software does not accommodate manufacturing constraints [2]. Therefore, substantial modifications are imposed on the optimized designs to make them manufacturable and hence render them nonoptimal. To make matters worse, Topology Optimized (TO) designs are geometrically complex and difficult to manufacture with traditional manufacturing processes. Fortunately, AM is able to accommodate such complexities, however, there are still restrictions [6, 7]. To these ends, research in TO for isotropic materials has incorporated AM constraints that quantify minimum feature size [8, 9, 10, 11], maximum feature size [12], self support requirements [6, 13, 7, 14, 15], and build direction. Support structure considerations is an especially active research topic. This is because support structures serve as building platforms and heat sinks that

reduce residual stress and deformation (e.g., distortion/curling) [16]. However, supports also increase manufacturing effort and cost [17]. Additional challenges such as the anisotropy induced by the layer-by-layer fabrication process, and the intrinsic anisotropy of the material warrant additional research [18].

Future research must further integrate TO designs with their manufacturing processes. For instance, TO designs require conversion to transform them to Stereo Lithography (STL) Computed Aided Design (CAD) models [6, 19]. Then, another software slices these CAD models into layers and generates the AM printer commands, e.g., the G-code used in Computer Numerical Control (CNC) machines.

Along with AM, other technologies such as Automated Tape Laying (ATL) and Advanced Fiber Placement (AFP) produce curvilinear fiber paths in composite structures. All these technologies produce structures with greater potential for mechanical performance improvements versus straight fiber laminates. As expected, however, curvilinear paths require more manufacturing restrictions than straight fiber laminates. These restrictions include constraints on path continuity, gaps, overlaps, maximum curvature, minimum cut length, fiber angle deviation, boundary smoothness and fiber bridging [2]. Despite the extensive study of structural optimization of variable stiffness composites, the integration of these manufacturing constraints into the design optimization problem is lacking [2].

Structural composite fiber optimization begins with discretizing the structure by finite elements. In the most naive approaches, the fiber orientation is optimized in each element. However, rapid changes of the optimized fiber orientations produce discontinuous fiber paths which cannot be manufactured. To overcome this, a post-processing step is required to produce continuous and manufacturable fiber paths that best fit the optimized fiber orientations; this step is nontrivial. To improve fiber path continuity, Abdalla et al. [20, 21, 22] use classical lamination theory and define the elasticity coefficients in terms of four nodal lamination parameters. The stiffness of the laminate is continuous, however, post-processing is required to obtain fiber paths. Setoodeh and Blom [23] retrieve the fiber paths from the stiffness distribution in a post-processing step using a curve fitting technique that imposes a curvature constraint. Later, Setoodeh et al. [24] use nodal rather than elemental fiber orientation parameters to obtain a continuous fiber orientation, however, the spatial derivatives and thus fiber curvature is discontinuous across the element boundaries. They also propose a heuristic pattern matching technique to improve manufacturability. Again in a post-processing technique, Blom et al. [25] use a streamline method to generate continuous fiber paths from the fiber orientation distribution. Kiyono et al. [26] filter the orientation distribution to improve smoothness, however, the fiber paths are still discontinuous due to the element-based discretization.

To ensure continuous fiber paths, researchers have replaced the finite element based fiber orientation descriptions with functional representations e.g., NURBS, Lagrangian polynomials, Bezier curves, constant angle and constant curvature paths [27, 28, 29, 30, 31, 32, 33, 34, 35, 36, 37]. To overcome overlap issues, Tatting et al. [38] use a post-processing tow-dropping method, however, this creates small wedge-like gap regions. Waldhart et al. [39, 40] define the fiber path by a curve that is parameterized by a single variable allowing them to satisfy a maximum curvature constraint. Other researchers [41, 42] define a point-wise curvature constraint via a single maximum curvature measure. However, it is well known that the non-differentiable max function produces numerical issues which inhibit the effectiveness of gradient-based optimization algorithms.

Brampton et al. [43] proposed a level-set method to describe continuously varying fiber paths that can be manufactured with AFP technology. This approach defines a primary fiber path as the zero level-set. Adjacent fiber paths are obtained from the primary path using the fast marching method [44]. This extrapolation obtains evenly spaced fiber paths, but discontinuities can appear, reducing manufacturability. The zero level-set, i.e., design, is updated with a Hamilton-Jacobi formulation using approximate sensitivities that are obtained using an energy-based method [45]. The inefficiency of the Hamilton-Jacobi formulation, and the approximated sensitivities, result in an optimization algorithm that convergences slowly and is highly dependent on the initial design, however, there is much potential offered from the level-set method.

Roberge and Norato [46] use element path spacing and orientation parameters to optimize curvilinear scaffolds that are fabricated via Direct Ink Writing (DIW). To obtain manufacturable toolpaths, they transform the path spacing and orientation distribution into a scalar field whose level-set contours represent the toolpaths. This post-processing transformation uses linear least squares and a smoothing filter.

Liu and Yu [47] integrate TO with the level-set description for path planning in the AM process. The zero level-set is interpreted as the domain boundary, and level-set contours in the domain are interpreted as toolpaths. A heuristic multi-step algorithm is required to overcome issues related to approximated sensi-

tivities. Liu and To [48] extended this work to three-dimensional structures subject to support constraints wherein, a multi-level-set interpolation ensures that the upper layers are supported by the lower layers. Again due to sensitivity approximations, the optimization algorithm exhibits poor convergence. All of these post-processes, yield fabricated parts that do not match the original TO designs; optimality is compromised. In our work, we ensure this does not occur.

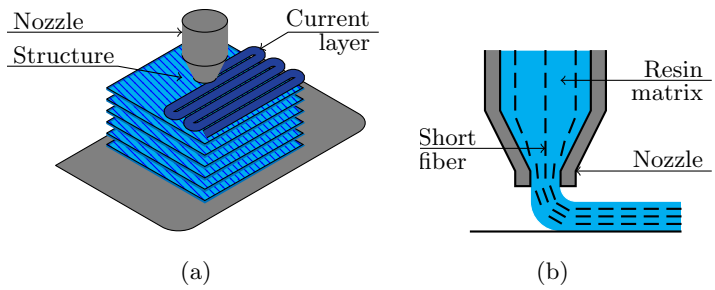

Figure 1: Schematic representation of the (a) DIW printing process and (b) short fiber alignment.

The enforcement of manufacturing constraints in the optimization should be effective and efficient. For example, implicit manufacturing constraints enforced with heuristic methods result in algorithms with poor convergence (e.g., the use of a fast marching method in [43]) and designs that do not necessarily satisfy the desired manufacturing constraints (e.g., the use of a filter in [26]). Explicit constraints are preferred. Our work integrates explicit manufacturing constraints into the optimization such that the resulting designs are readily manufacturable.

We propose to optimize the design of Fiber Reinforced Composite (FRC) structures that are amenable to AM. The process of our study uses DIW wherein a thermoset resin which contains short carbon fibers is extruded through a moving nozzle and quickly cured or semi-cured thereby forming the FRC structure [49], cf. Figure 1. During the extrusion, the fibers orient themselves with the flow direction and, as reported in [49] an 8 vol.% of carbon fibers in an FRC manufactured using this DIW technique has a directional Young's Modulus that is 37% higher than the equivalent FRC with randomly oriented carbon fibers. Thus, we have the ability to tailor the structural properties by tailoring the toolpath trajectory. However, not all toolpaths are realizable, e.g., the paths on each layer cannot overlap and for correct alignment of the fibers the toolpath cannot change direction abruptly. To accommodate these DIW fabrication restrictions, we define the toolpaths of each printed layer by the contours of a level-set function. The level-set surface is defined from a B-surface and the heights of the B-surface control points serve as the design variables in the optimization. This parametrization allows us to explicitly define the DIW constraints and the structural mass and stiffness. We apply this technique to minimize the compliance of three-dimensional FRC structures fabricated via DIW. We perform sensitivity analysis with respect to the level-set parametrization, making it amenable to gradient-based optimization algorithms which exhibit fast convergence and satisfy the optimality conditions.

The optimal toolpaths for our optimized design start and stop at the domain boundary, cf. Figure 10. To enable the DIW process, we must link these start and stop boundary points together to form a continuous path. And to minimize manufacturing time, we want the shortest path. To these ends, we formulate and solve a Traveling Salesman Problem (TSP). Having the shortest layer toolpaths, we generate the G-code for the DIW path planning. Optimized designs can then be readily validated via fabrication and testing, we do such validations.

The remainder of the paper is organized as follows. In Section 2, we describe the toolpath parametrization using level-sets. Section 3 explains the imposition of the DIW constraints. In Section 4, we present the material model. We discuss the elastostatic and optimization problems in Sections 5 and 6 respectively. In Section 7, we explain how to generate the optimized G-code from the level-set function. The numerical implementation and examples are provided in Section 8. We conclude in Section 9.

2 Parametrization

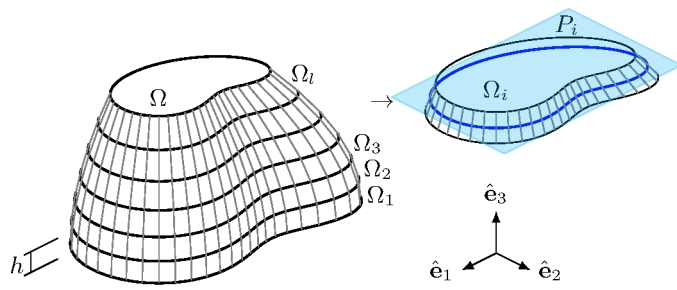

Figure 2: Domain Ω divided into n_l layer domains Ω_i.

The DIW process prints the structural domain Ω layer by layer from bottom to top. Essentially, we slice Ω into n_l layers of thickness h to form the layer domains, $\Omega_1, \Omega_2, ..., \Omega_l$, that are stacked in the $\hat{\mathbf{e}}_3$ direction, cf. Figure 2, such that $\Omega_i = \{\mathbf{x} \in \Omega \,|\, (i-1)\,h < \mathbf{x} \cdot \hat{\mathbf{e}}_3 < i\,h\}$.

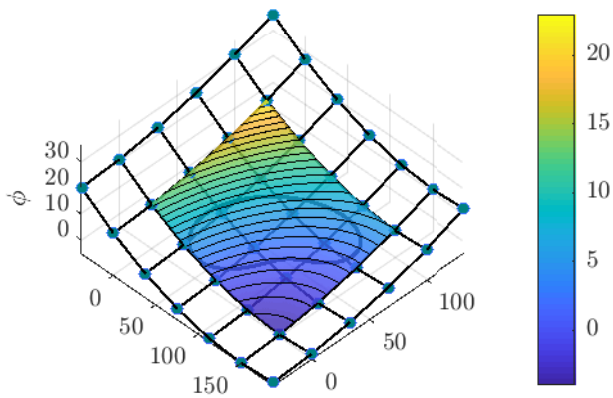

Figure 3: A level-set function ϕ_i defined by a rectangular grid of 7×6 control points.

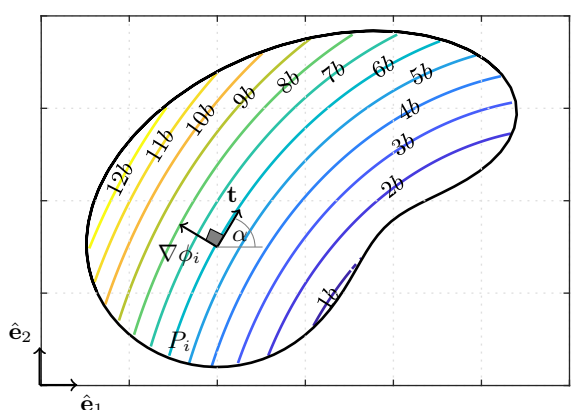

Figure 4: $\mathcal{C}_i^k$ contours of level-set function ϕ_i.

We define the toolpaths for the layer Ω_i at its mid-plane $P_i = \{\mathbf{x} \in \Omega_i \,|\, \mathbf{x} \cdot \hat{\mathbf{e}}_3 = (i-1)h + h/2\}$. The

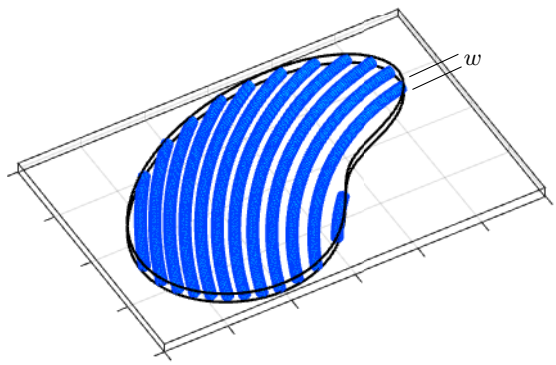

Figure 5: Spatial view of material deposited.

toolpath centerlines $\mathcal{C}_i^k$ for each layer Ω_i are represented implicitly by the contours of a level-set function ϕ_i

$$\mathcal{C}_i^k = \{\, \mathbf{x} \mid \phi_i(\mathbf{x}) = k\, b\}, \quad k \in \mathbb{Z}. \tag{1}$$

The contour values $k\, b$ that define the toolpaths are integer multiples of an arbitrary parameter b. In Figure 4, we show a set of contours $\phi_i(\mathbf{x}) = 1b$, $2b$,..., $12b$, where each color represents a different level. In Figure 5, we see how the deposited material of width w will look if we follow the toolpaths represented by these contours. For convenience and without loss of generality, we choose $b = w$.

The level-set function $\phi_i : P_i \to \mathbb{R}$ for the layer Ω_i is defined over the plane P_i by $\phi_i(\mathbf{x}) = \mathbf{d}_i^\mathsf{T}\, \hat{\mathbf{N}}(\mathbf{x})$, where the vector of basis functions is $\hat{\mathbf{N}}(\mathbf{x}) = [\hat{N}_1(\mathbf{x}), \hat{N}_2(\mathbf{x}), ..., \hat{N}_n(\mathbf{x})]^\mathsf{T} \in \mathbb{R}^n$ and the vector of control point height parameters is $\mathbf{d}_i = [d_{i1}, d_{i2}, ..., d_{in}]^\mathsf{T} \in \mathbb{R}^n$ (cf. Figure 3 and Appendix A). The latter serve as the design variables in the optimization.

As discussed in Section 3, to accommodate the DIW constraints, we require a $\mathcal{C}^2$-continuous level-set function ϕ_i. This smoothness guarantees continuous toolpaths with no jumps in curvature. Cubic B-splines are $\mathcal{C}^2$-continuous curves defined with piecewise cubic polynomials. For this reason, we represent the level-set functions using B-surfaces constructed with bi-cubic B-splines. And for convenience, we define the B-surface over a fixed rectangular grid of control points. In this way, the design description is independent of the finite element mesh that we use for structural analysis. Designs are not invariant with respect to the orientation of the rectangular grid of control points, however, this effect can be neglected for a smooth function and/or a sufficiently refined grid. Moreover, large changes in the curves can be obtained without the addition or subtraction of control points as opposed to explicit curve definitions [50, 51]. The B-spline toolpath definition allows for internal loops, however in our method, manufacturing constraints prohibit this possibility, cf. Section 3. With this parameterization, we drastically reduce the number of design variables versus finite element based parameterization schemes and we ensure the toolpaths on each layer are smooth and well spaced.

The toolpath orientation is a function of the level-set function ϕ_i. To see this, we define derivatives of the basis functions as $\hat{\mathbf{B}}_1 = (\partial\hat{\mathbf{N}}/\partial x_1)^\mathsf{T}$ and $\hat{\mathbf{B}}_2 = (\partial\hat{\mathbf{N}}/\partial x_2)^\mathsf{T}$, and calculate the gradient of the level-set function

$$\nabla\phi_i(\mathbf{x}) = \begin{bmatrix} \frac{\partial\phi_i(\mathbf{x})}{\partial x_1} \\ \frac{\partial\phi_i(\mathbf{x})}{\partial x_2} \end{bmatrix} = \begin{bmatrix} \hat{\mathbf{B}}_1(\mathbf{x}) \\ \hat{\mathbf{B}}_2(\mathbf{x}) \end{bmatrix} \mathbf{d}_i\,. \tag{2}$$

Next, we let $\mathbf{r}_i^k(t)$ be any parametrization of the toolpath $\mathcal{C}_i^k$. By the chain rule $\mathrm{d}\phi_i(\mathbf{r}_i^k(t))/\mathrm{d}t = \nabla\phi_i(\mathbf{r}_i^k(t)) \cdot \mathrm{d}\mathbf{r}_i^k(t)/\mathrm{d}t = 0$, which implies $\nabla\phi_i(\mathbf{r}_i^k)$ is perpendicular to the path tangent vector $\mathbf{t}_i^k(t) = \mathrm{d}\mathbf{r}_i^k(t)/\mathrm{d}t$ (see Figure 4), where

$$\mathbf{t}_i^k(t) = \frac{1}{|\nabla\phi_i(\mathbf{r}_i^k(t))|} \begin{bmatrix} \frac{\partial\phi_i(\mathbf{r}_i^k(t))}{\partial x_2} \\ -\frac{\partial\phi_i(\mathbf{r}_i^k(t))}{\partial x_1} \end{bmatrix} = \frac{1}{|\nabla\phi_i(\mathbf{r}_i^k(t))|} \begin{bmatrix} \hat{\mathbf{B}}_2(\mathbf{r}_i^k(t)) \\ -\hat{\mathbf{B}}_1(\mathbf{r}_i^k(t)) \end{bmatrix} \mathbf{d}_i\,. \tag{3}$$

The toolpath orientation angle α is given by the inclination of $\mathbf{t}$ with respect to the $\hat{\mathbf{e}}_1$ axis as seen in Figure 4, i.e., $\alpha_i^k(t) = \mathrm{atan2}\left(-\partial\phi_i(\mathbf{r}_i^k(t))/\partial x_1, \partial\phi_i(\mathbf{r}_i^k(t))/\partial x_2\right)$. Generalizing this, we define the orientation angle

at any point $\mathbf{x}$ by

$$\alpha_i(\mathbf{x}) = \text{atan2}\left(-\frac{\partial \phi_i(\mathbf{x})}{\partial x_1}, \frac{\partial \phi_i(\mathbf{x})}{\partial x_2}\right), \tag{4}$$

cf. Figure 6. In the above, $\text{atan2}(a_1, a_2)$ is the arctangent function of the two arguments a_1 and a_2 that returns the angle α such that $\sin(\alpha) = a_1/\sqrt{a_1^2 + a_2^2}$ and $\cos(\alpha) = a_2/\sqrt{a_1^2 + a_2^2}$.

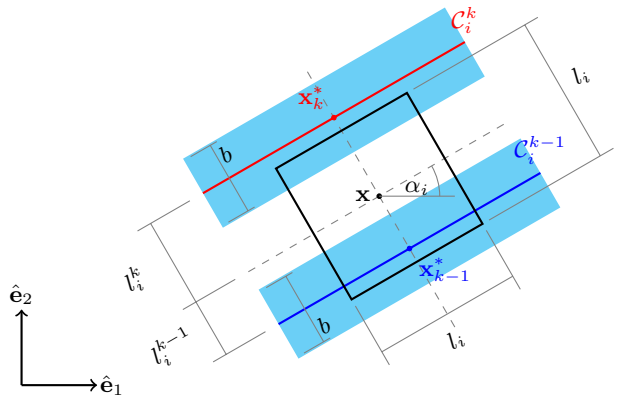

Figure 6: Distance between toolpaths and representative volume element.

As discussed in Section 3, overlap and sagging constraints are functions of the distance between the toolpaths. To evaluate the distance between adjacent toolpaths $\mathcal{C}_i^k$ and $\mathcal{C}_i^{k-1}$ at the point $\mathbf{x}$ in each layer Ω_i (cf. Figure 6), we must find the closest point $\mathbf{x}_k^*$ on the path $\mathcal{C}_i^k$ to $\mathbf{x}$; it is the $\mathbf{y}$ that solves the minimization problem

$$\begin{aligned} \min_{\mathbf{y}} \quad & |\mathbf{y} - \mathbf{x}|^2 \\ \text{subject to} \quad & \phi_i(\mathbf{y}) = k\, b. \end{aligned} \tag{5}$$

The solution to the above satisfies the Karush-Kuhn-Tucker (KKT) optimality conditions

$$2(\mathbf{x}_k^* - \mathbf{x}) + \lambda^* \nabla \phi_i(\mathbf{x}_k^*) = \mathbf{0} \tag{6}$$

$$\phi_i(\mathbf{x}_k^*) - k\, b = 0 \tag{7}$$

where λ is the Lagrange multiplier. However, we instead define $\mathbf{x}_k^* = \mathbf{x} + \Delta\mathbf{x}_k$ and assume $\Delta\mathbf{x}_k$ and $\lambda^* \nabla^2 \phi_i(\mathbf{x}) \Delta\mathbf{x}_k$ are small. Whence the first order Taylor series expansions give

$$\phi_i(\mathbf{x}_k^*) \approx \phi_i(\mathbf{x}) + \nabla\phi_i(\mathbf{x}) \cdot \Delta\mathbf{x}_k\,, \tag{8}$$

$$\nabla\phi_i(\mathbf{x}_k^*) \approx \nabla\phi_i(\mathbf{x}) + \nabla^2\phi_i(\mathbf{x})\Delta\mathbf{x}_k\,. \tag{9}$$

which when combined with Equations (6) and (7), gives

$$\Delta\mathbf{x}_k \approx \frac{k\, b - \phi_i(\mathbf{x})}{|\nabla\phi_i(\mathbf{x})|^2} \nabla\phi_i(\mathbf{x}). \tag{10}$$

The closest point on the toolpath $\mathcal{C}_i^{k-1}$ to $\mathbf{x}$ is similarly approximated as $\mathbf{x}_{k-1}^* = \mathbf{x} + \Delta\mathbf{x}_{k-1}$ where

$$\Delta\mathbf{x}_{k-1} \approx -\frac{(k-1)\, b - \phi_i(\mathbf{x})}{|\nabla\phi_i(\mathbf{x})|^2} \nabla\phi_i(\mathbf{x}). \tag{11}$$

Finally, the distance between the two toolpaths $\mathcal{C}_i^k$ and $\mathcal{C}_i^{k-1}$ at $\mathbf{x}$, is approximated as

$$l_i = |\Delta\mathbf{x}_k + \Delta\mathbf{x}_{k-1}| \approx \frac{b}{|\nabla\phi_i|}. \tag{12}$$

i.e., the spacing between toolpaths depends on the gradient of the level-set function. We use the spacing between toolpaths and the toolpath orientation angle in the following sections to define the DIW constraints and the material model.

3 DIW constraints

As mentioned in the previous section, the spacing between toolpaths is related to the gradient of the level-set function. Even spacing between toolpaths indicates the level-set function has a uniform gradient. Closely spaced toolpaths are indicative of large $|\nabla\phi_i|$ values, whereas widely spaced toolpaths are indicative of small values.

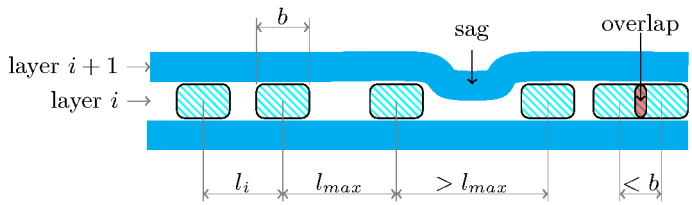

Figure 7: Cross-section of layer i showing overlap and maximum distance between tool-paths to prevent sag of top layer.

In Figure 7, we show the cross-section of the printed paths of a layer i. Notice that the minimum allowed distance between toolpaths is b. So, toolpaths do not overlap if $l_i \geq b$. Using Equation (12), we express this no-overlap constraint by

$$|\nabla\phi_i(\mathbf{x})| \leq 1. \tag{13}$$

This constraint must be enforced for every point $\mathbf{x}$ in each layer Ω_i, i.e., it is a local constraint.

To consolidate local constraints into a single global constraint, we mimic Amstutz et al. [52] and express one overlap global constraint for each layer Ω_i as

$$G_i^a = \int_{P_i} R(|\nabla\phi_i|^2 - 1)\,\mathrm{d}a \leq 0\,, \tag{14}$$

where R is a ramp function such that

$$R(\theta) = \begin{cases} 0, & \text{if } \theta \leq 0 \\ m\,\theta, & \text{if } \theta > 0\,, \end{cases} \tag{15}$$

where $m > 0$. It is easily seen that if, for some region in the domain, $|\nabla\phi_i| > 1$, then the constraint is violated, i.e., $G_i^a > 0$. We thus have one overlap constraint per layer. It is also possible to aggregate the layer-wise constraints into a single constraint $G^a = \sum G_i^a$, similar to the aggregation of stress constraints for multiple load cases in [53].

To use gradient-based methods to solve the optimization problem, we redefine R as the continuous differentiable piecewise function

$$R(\theta) = \begin{cases} 0, & \text{if } \theta \leq -\delta \\ m\left(\frac{\theta^3}{6\delta^2} + \frac{\theta^2}{2\delta} + \frac{\theta}{2} + \frac{\delta}{6}\right), & \text{if } -\delta < \theta \leq 0 \\ m\left(-\frac{\theta^3}{6\delta^2} + \frac{\theta^2}{2\delta} + \frac{\theta}{2} + \frac{\delta}{6}\right), & \text{if } 0 < \theta \leq \delta \\ m\,\theta, & \text{if } \delta < \theta \end{cases} \tag{16}$$

where a smaller δ corresponds to a sharper transition at $\theta = 0$, cf. Figure 8. The coefficients m and δ must be chosen such the numerical optimization is stable.

To enforce evenly spaced toolpaths, researchers [43, 47] extrapolate the zero level-set using the fast marching method [44]. As mentioned in the introduction, this extrapolation does not always guarantee continuous paths. If required, a no gap constraint can be added to the problem formulation by enforcing the separation between the toolpaths to be constant (i.e., $l = b$ or $|\nabla\phi| = 1$). However, the toolpaths do not need to be evenly spaced in our DIW process. That said, if no volume constraint is imposed, somewhat evenly

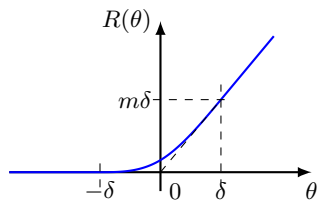

Figure 8: Approximate ramp function.

spaced toolpaths naturally appear in the designs produced in the Results Section because the optimizer wants a stiffer, fully dense, structure.

In DIW processes the extruded material sags if it does not have proper support, cf. Figure 7, especially if the printed material cures slowly. To prevent sag, we consider the two adjacent toolpaths $\mathcal{C}_i^k$ and $\mathcal{C}_i^{k-1}$ on layer Ω_i illustrated in Figure 9. Line AC, represents a portion of the layer Ω_{i+1} toolpath $\mathcal{C}_{i+1}^j$ immediately above toolpaths $\mathcal{C}_i^k$ and $\mathcal{C}_i^{k-1}$. As seen in the figure, points A and C on layer Ω_i support $\mathcal{C}_{i+1}^j$ on layer Ω_{i+1}. The distance between these support points at $\mathbf{x} \in \Omega_i$ is approximated by

$$l_{AC} = \frac{l_i}{\left|\sin\left(\alpha_{i+1}^j - \alpha_i^{k-1}\right)\right|}, \tag{17}$$

where l_i is the Equation (12) approximated distance between toolpaths $\mathcal{C}_i^k$ and $\mathcal{C}_i^{k-1}$, and α_{i+1}^j and α_i^{k-1} are the orientation angles of toolpaths $\mathcal{C}_{i+1}^j$ and $\mathcal{C}_i^{k-1}$ at A. We approximate these angles by $\alpha_{i+1}^j \approx \alpha_{i+1}(\mathbf{x})$ and $\alpha_i^{k-1} \approx \alpha_i(\mathbf{x})$. Sag occurs if l_{AC} is larger than the maximum allowed distance l_{max}, and thus at each $\mathbf{x} \in \Omega_i$ we require $l_{AC} \leq l_{max}$. These local no-sag constraints are agglomerated for each layer Ω_i as

$$G_i^b = \int_{P_i} R\left(1 - \frac{l_{max}^2}{b^2}|\nabla\phi_i|^2 \sin^2\left(\alpha_{i+1} - \alpha_i\right)\right) \mathrm{d}a \leq 0\,, \tag{18}$$

where R is the smooth ramp function of Equation (16) and we use Equations (4), (12), and (17) to express α_i and α_{i+1} in terms of ϕ_i and ϕ_{i+1}.

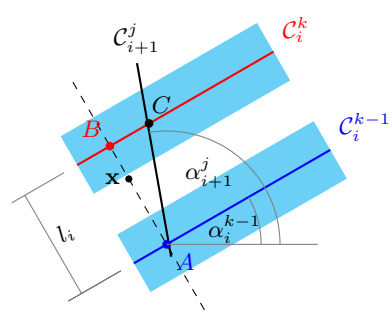

Figure 9: Support points A and C in toolpaths $\mathcal{C}_i^{k-1}$ and $\mathcal{C}_i^k$ for upper toolpath $\mathcal{C}_{i+1}^j$.

The G_i^b no-sag constraints, forces toolpaths to be closely spaced on each layer, and to form a cross-pattern with respect of the toolpaths of their adjacent layers. And because $0 \leq \sin^2\left(\alpha_{i+1} - \alpha_i\right) \leq 1$, the slope of the level-set function is bounded from below as $|\nabla\phi(\mathbf{x})| \geq b/l_{max}$. An important consequence of this constraint is that toolpaths cannot form internal loops, guaranteeing continuous toolpaths across the domain. Using a similar argument with Equations (12), (13) and (17), we determine that the angle difference between the toolpaths of the adjacent layers is bounded by

$$|\alpha_{i+1} - \alpha_i| \geq \sin^{-1}\left(\frac{b}{l_{max}}\right) > 0, \tag{19}$$

i.e., toolpaths on an upper layer should not be parallel to the toolpaths of its supporting layer. This constraint further enforces a well-supported cross-pattern between adjacent layers.

Manufacturable toolpaths have a minimum allowable radius of curvature r_{min} because in regions with small radius of curvature, the fibers do not align with the toolpath. To satisfy this minimum radius of curvature constraint, we compute the path curvature κ_i via the divergence of the curve $\mathcal{C}_i^k$ normal vector, i.e., $\kappa_i = \nabla \cdot \mathbf{n}_i$, where $\mathbf{n}_i = \nabla\phi_i/|\nabla\phi_i|$. For our level-set representation this reduces to

$$\kappa_i = \nabla . \frac{\nabla\phi_i}{|\nabla\phi_i|} = \frac{\frac{\partial^2\phi_i}{\partial x_1^2}\left(\frac{\partial\phi_i}{\partial x_2}\right)^2 - 2\frac{\partial^2\phi_i}{\partial x_1\partial x_2}\left(\frac{\partial\phi_i}{\partial x_1}\right)\left(\frac{\partial\phi_i}{\partial x_2}\right) + \frac{\partial^2\phi_i}{\partial x_2^2}\left(\frac{\partial\phi_i}{\partial x_1}\right)^2}{|\nabla\phi_i|^3}\,, \tag{20}$$

where the second derivatives are computed by differentiating Equation (2).

The curvature is continuous since we require $\phi_i \in \mathcal{C}^2$. This is ensured by using bi-cubic B-splines to define ϕ_i. Jumps in curvature are prohibited, but the radius of curvature can adopt any value $r_i = |\kappa_i|^{-1} > 0$ hence we enforce a minimum curvature constraint $|\kappa_i^{-1}| \geq r_{min}$ via the layer Ω_i global curvature constraint

$$G_i^c = \int_{P_i} R(r_{min}^2\,\kappa_i^2 - 1)\,\mathrm{d}a \leq 0\,. \tag{21}$$

This constraint also eliminates the rapid changes in the fiber orientations which often appear in finite element based parameterizations [24].

4 Material modeling

The printed structure is modeled as a variable stiffness composite laminate in which the material volume fraction and stiffness are homogenized in terms of our level-set function. To approximate the volume fraction of the material at $\mathbf{x} \in \Omega_i$, we introduce a rectangular parallelepiped as a Representative Volume Element (RVE) of size $l_i \times l_i \times h$ oriented with the angle α with respect to the $\hat{\mathbf{e}}_1$ axis, cf. Figure 6. In this RVE, we assume the toolpaths are parallel. Thus, the minimum radius of curvature constraint also helps to maintain the integrity of our RVE formulation as we minimally require $r_{min} > l_{max}$. As seen in the Figure 6, $\mathbf{x}_k^* \in \mathcal{C}_i^k$ and $\mathbf{x}_{k-1}^* \in \mathcal{C}_i^{k-1}$ are the closest toolpath points to $\mathbf{x}$, and l_i^k and l_i^{k-1} are their respective distances from $\mathbf{x}$. The lateral RVE dimension $l_i = l_i^k + l_i^{k-1}$ is the distance between the toolpaths. Using Equation (12), we compute the volume fraction of material enclosed in the RVE at $\mathbf{x} \in \Omega_i$ as

$$\nu_i \approx \frac{b\,l_i\,h}{l_i^2\,h} = |\nabla\phi_i|\,. \tag{22}$$

We compute the total volume fraction of the design as

$$\nu_T = \frac{1}{V_\Omega}\sum_{i=1}^{n_l}\int_{\Omega_i}\nu_i(\mathbf{x})\,\mathrm{d}v\,, \tag{23}$$

where V_Ω is the total volume of the domain Ω.

We homogenize the stiffness in the layer Ω_i at each point $\mathbf{x}$ using the volume fraction, ν_i, and the fiber orientation α_i, i.e.,

$$\mathbb{C}_i^*(\mathbf{x}) = \nu_i(\mathbf{x})\,\mathbb{C}(\alpha_i(\mathbf{x}))\,, \tag{24}$$

where

$$\mathbb{C}(\alpha) = (\mathbf{R}_z(\alpha) \boxtimes \mathbf{R}_z(\alpha))\;\mathbb{C}_0\;(\mathbf{R}_z(\alpha) \boxtimes \mathbf{R}_z(\alpha))^{\mathsf{T}}\,, \tag{25}$$

$\mathbb{C}_0$ is the stiffness of the full volume fraction material with fibers parallel to $\hat{\mathbf{e}}_1$, $\mathbf{R}_z$ is an α rotation tensor about the $\hat{\mathbf{e}}_3$ axis, and $\boxtimes$ represent the conjugation product with components $(\mathbf{A} \boxtimes \mathbf{B})_{ijkl} = A_{ik}B_{jl}$. The material properties for each layer Ω_i vary in the plane P_i; they are uniform in the $\hat{\mathbf{e}}_3$ direction. See Appendices B and C for further details. Adjacent layers, i.e., Ω_{i+1} and Ω_{i-1}, may have interfacial stiffness with Ω_i, however our analysis assumes full adhesion between layers, cf. Appendix D.

The sensitivity of the stiffness is given by

$$\frac{\partial \mathbb{C}_i^*}{\partial \mathbf{d}_i} = \frac{\partial \nu_i}{\partial \mathbf{d}_i}\,\mathbb{C} + \nu_i\,\frac{\partial \mathbb{C}}{\partial \alpha_i}\,\frac{\partial \alpha_i}{\partial \mathbf{d}_i}\,, \tag{26}$$

where the components of $\partial\mathbb{C}/\partial\alpha_i$ are provided in the Appendix C. The derivative of the orientation angle with respect to the design variables follows from Equations (2) and (4), i.e.,

$$\frac{\partial \alpha_i}{\partial \mathbf{d}_i} = \frac{\frac{\partial \phi_i}{\partial x_1}\hat{\mathbf{B}}_2 - \frac{\partial \phi_i}{\partial x_2}\hat{\mathbf{B}}_1}{|\nabla \phi_i|^2}\,. \tag{27}$$

The derivative of the volume fraction follows from Equations (2) and (22)

$$\frac{\partial \nu_i}{\partial \mathbf{d}_i} = \frac{\frac{\partial \phi_i}{\partial x_1}\hat{\mathbf{B}}_1 + \frac{\partial \phi_i}{\partial x_2}\hat{\mathbf{B}}_2}{|\nabla \phi_i|}\,. \tag{28}$$

5 Elastostatics

The governing equations for the displacement $\mathbf{u}$ of our linear elastic body are

$$\begin{aligned}
\operatorname{div}\boldsymbol{\sigma} + \mathbf{f}^b &= \mathbf{0} && \text{in } \Omega\,,\\
\boldsymbol{\sigma} &= \mathbb{C}_i^*\,\boldsymbol{\epsilon} && \text{in } \Omega_i \quad \text{for} \quad i = 1, 2, ..., n_l\,,\\
\boldsymbol{\epsilon} &= (\nabla\mathbf{u} + \nabla\mathbf{u}^{\mathsf{T}})/2 && \text{in } \Omega\,,\\
\mathbf{u} &= \mathbf{0} && \text{on } \Gamma^u\,,\\
\boldsymbol{\sigma}\,\mathbf{n} &= \mathbf{f}^t && \text{on } \Gamma^t\,,\\
\boldsymbol{\sigma}\,\mathbf{n} &= \mathbf{0} && \text{on } \Gamma^0\,,
\end{aligned} \tag{29}$$

where $\mathbf{f}^b$ is the body force, $\boldsymbol{\sigma}$ and $\boldsymbol{\epsilon}$ are the stress and strain tensors, $\mathbf{n}$ is the normal vector to the domain boundary $\partial\Omega$. The displacement is fixed on the boundary Γ^u and the traction $\mathbf{f}^t$ is prescribed on Γ^t and zero over $\Gamma^0 = \partial\Omega \setminus (\Gamma^u \cup \Gamma^t)$.

In this study, the cost function is the usual compliance, i.e.,

$$c = \int_\Omega \mathbf{u}\cdot\mathbf{f}^b\,\mathrm{d}v + \int_{\Gamma^t} \mathbf{u}\cdot\mathbf{f}^t\,\mathrm{d}a\,. \tag{30}$$

Using the adjoint method, the sensitivities are (cf. [54, 55])

$$\frac{Dc}{D\mathbf{d}_i} = -\int_{\Omega_i} \boldsymbol{\epsilon}^{\mathsf{T}}\,\frac{\partial \mathbb{C}_i^*}{\partial \mathbf{d}_i}\,\boldsymbol{\epsilon}\,\mathrm{d}v. \tag{31}$$

Note that we compute this integral for each layer Ω_i to evaluate the sensitivities with respect to its layer Ω_i design variable vector $\mathbf{d}_i$.

6 Optimization problem

As mentioned above, our goal is to design an FRC structure that minimizes compliance and satisfies manufacturing constraints. To these ends, we solve the optimization problem

$$\begin{aligned}
\min_{\mathbf{d}} \quad & c\\
\text{subject to} \quad & \nu_T \le \nu_{max},\\
& G_i^a \le 0, \qquad i = 1, 2, ..., n_l\\
& G_i^b \le 0, \qquad i = 1, 2, ..., n_l - 1\\
& G_i^c \le 0. \qquad i = 1, 2, ..., n_l
\end{aligned} \tag{32}$$

where ν_{max} is the maximum allowable total volume fraction.

We use the nonlinear programming software IPOPT [56] to solve the optimization problem. Exact sensitivities are provided to this optimizer to solve the problem accurately and efficiently. In the previous section, we described how to evaluate sensitivities of the compliance cost function. The sensitivity computation of the constraints is straightforward as they are explicit functions of $\mathbf{d}$.

It is well known that nonlinear programming optimizers usually converge to local minimizers, making the initial design very important. We start from a feasible design in which each layer is made of parallel-straight toolpaths with volume fraction $\nu = \nu_{max}$. To do this, we define the layer vectors $\mathbf{a}_i = \nu_{max}\,[-\sin(\alpha_i), \cos(\alpha_i), 0]^\mathsf{T}$ and $\phi_i = \mathbf{a}_i \cdot \mathbf{x}$ so that $\nabla\phi_i = \mathbf{a}_i$ is uniform and $|\nabla\phi_i| = |\mathbf{a}_i| = \nu_{max}$. We then solve the optimization problem

$$\begin{aligned} \min_{\alpha_1,\alpha_2,\ldots,\alpha_{nl}} \quad & c \\ \text{subject to} \quad & G_i^0 \leq 0 \quad i = 1, 2, ..., n_l - 1 \end{aligned} \tag{33}$$

where

$$G_i^0 = 1 - \frac{l_{max}^2}{b^2}\nu_{max}^2 \sin^2(\alpha_{i+1} - \alpha_i) \leq 0. \tag{34}$$

is the no-sag constraint, cf. Equation (18). The solution of Equation (33) i.e., optimal layer angles α_i, is used to define the initial design variables $\mathbf{d}_i$ such that $(d_i)_j = \phi_i(\mathbf{x}_j) = \mathbf{a}_i \cdot \mathbf{x}_j$ where $\mathbf{x}_j$ are the control point coordinates for layer Ω_i.

7 G-code generation

Since $|\nabla\phi_i| > 0$, we are assured the level-set contours on each layer Ω_i are continuous and contain no loops (cf. Section 3). As such, the toolpaths start and finish at a boundary and we need to link them to form a continuous toolpath to generate the layer Ω_i G-code. Ideally, we would like the shortest toolpath possible so as to minimize production time and waste, i.e., amount of trimmed material. Traditional zigzag (cf. Figure 10a) and one-way (cf. Figure 10b) methods to connect the contours generally do not obtain the shortest continuous toolpath [57] especially if there are holes. To address this path generation problem, we formulate and solve a TSP. Given a finite number of cities and the cost of travel between each pair of cities, the solution of the TSP finds the cheapest route of visiting each city once and returning to the starting city. To formulate the linking sequence of the toolpaths as a TSP, we must define the cities and the cost of travel between them.

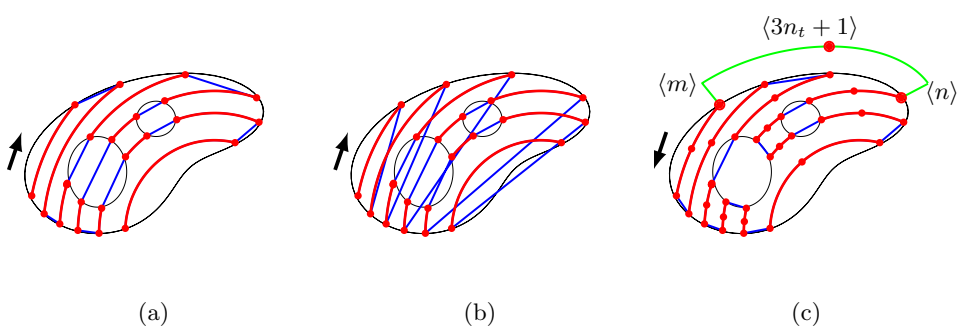

Figure 10: (a) Zigzag linking method, (b) One-way linking method, and (c) TSP solution. First, last and dummy cities are $\langle m\rangle$, $\langle n\rangle$ and $\langle 3n_t + 1\rangle$ respectively.

In our TSP formulation the first and last points of each toolpath $\mathcal{C}_i^k$ are the cities $\langle k\rangle$ and $\langle n_t + k\rangle$ respectively. We formulate a symmetric TSP where the cost of travel between the cities $\langle k\rangle$ and $\langle j\rangle$ is their distance $c_{k,j} = c_{j,k} = d(\mathbf{x}_k, \mathbf{x}_j)$. Additionally, we define a halfway city $\langle 2n_t + k\rangle$ located in between the first $\langle k\rangle$ and last $\langle n_t + k\rangle$ cities of each toolpath $\mathcal{C}_i^k$. Figure 10c depicts the cities and halfway cities with red dots and the printing direction with black arrows. To ensure that the toolpath follows each $\mathcal{C}_i^k$, we define

the distances such that $c_{2n_t+k,j} = c_{2n_t+k,n_t+j} = c_{2n_t+k,2n_t+j} = D_k^j$, where

$$D_k^j = \begin{cases} 0, & \text{if} \quad j = k \\ d_\infty, & \text{if} \quad j \neq k\,, \end{cases} \tag{35}$$

such that $d_\infty \gg 1$ is a large number. These distance definitions ensure that we respectively visit the cities along each toolpath $\mathcal{C}_i^k$ in the order $\langle k\rangle, \langle 2n_t + k\rangle, \langle n_t + k\rangle$ or visa versa $\langle n_t + k\rangle, \langle 2n_t + k\rangle, \langle k\rangle$.

The first and last point of each trajectory $\mathcal{C}_i^k$ belongs to the boundary ∂P_i, which may be the external boundary ∂P_i^E, or a hole boundary $\partial P_i^{H1}, \partial P_i^{H2}, ..., \partial P_i^{Hn_h}$, where n_h is the number of holes. To avoid connecting hole boundary cities to external boundary cities, we impose $c_{j,k} = d_\infty$ if $\mathbf{x}_j \in \partial P_i^{Hr}$ and $\mathbf{x}_k \in \partial P_i^E$. Similarly to avoid connecting cities on different hole boundaries, we define $c_{j,k} = d_\infty$ if $\mathbf{x}_j \in \partial P_i^{Hr}$, $\mathbf{x}_k \in \partial P_i^{Hs}$ for $r \neq s$.

Since we do not need to start and finish in the same city, we add a dummy city $\langle 3n_t + 1\rangle$ with the following distance definition

$$c_{3n_t+1,j} = \begin{cases} 0, & \text{if} \quad \mathbf{x}_j \in \partial P_i^E \\ d_\infty, & \text{otherwise.} \end{cases} \tag{36}$$

In this way, two ∂P_i^E boundary cities $\langle m\rangle$ and $\langle n\rangle$ are connected to the dummy city $\langle 3n_t + 1\rangle$. These cities $\langle m\rangle$ and $\langle n\rangle$ are the first and last cities visited and the path connecting them is $\langle m\rangle$, $\langle 3n_t + 1\rangle$, $\langle n\rangle$ (cf. Figure 10c).

Our TSP has $3n_t + 1$ cities and the symmetric cost matrix $c_{j,k}$ which is computed using the above definitions. To solve the TSPs, we use the efficient TSP solver Concorde [58]. Once we have the shortest toolpaths, we can readily write the G-code that guides the AM printer.

8 Examples

We apply our optimization method to generate five designs using the composite material described in Appendix B. The thickness of the layers and toolpaths are $h = 0.3\,\text{mm}$ and $b = 0.6\,\text{mm}$. We model the structures using (8-noded) tri-linear prismatic elements in the NIKE3D finite element software [59]. For numerical integration, NIKE3D uses a $2 \times 2 \times 2$ Gauss quadrature for each element. The level-set function for each layer is modeled using bi-cubic B-splines with patch size $10\,\text{mm} \times 10\,\text{mm}$ (cf. Appendix A) unless otherwise stated. For the numerical integration of the constraints, we use a 16×16 Gauss quadrature over each B-surface patch. The parameters of the smooth ramp function R are $\delta = 0.01$ and $m = 10$, the maximum sag distance is $l_{max} = 1.6\,\text{mm}$ and the minimum radius of curvature is $r_{min} = 2\,\text{mm}$ which is larger than l_{max}. We compute the compliance c_0 for a design with horizontal minimally spaced parallel toolpaths, i.e., $\phi_i(\mathbf{x}) = \mathbf{x} \cdot \hat{\mathbf{e}}_2$ for $i = 1, 2, ..., n_l$. We use this reference compliance c_0 to normalize the objective function. IPOPT converges successfully if the norm of the KKT optimality condition, is smaller than the tolerance $\epsilon_{\text{tol}} = 10^{-4}$ (cf. Equation (5) and (6) in [56]), unless otherwise stated.

8.1 Short cantilever beam

Our first example is a 2 layer short cantilever beam with dimensions shown in Figure 11a. The beam is subject to a transverse tip line load $\mathbf{f} = -1\,\text{kN/mm}\,\hat{\mathbf{e}}_2$ in the middle of the right face. The left face of the beam is fixed $\mathbf{u}(x_1 = 0) = \mathbf{0}$. The finite element mesh has 400 elements of size $1\,\text{mm} \times 1\,\text{mm} \times 0.3\,\text{mm}$. We model the level-set functions with 1×2 B-surface patches per layer, so the optimization problem has $(1 + 3)(2 + 3) = 20$ design parameters per layer, cf. Figure 11b. No volume restriction is imposed, i.e., $\nu_{max} = 1$.

To find the optimal solution for this short cantilever beam, we start with the initial angle orientation of $\pm 45^\circ$ for each layer and solve Equation 33 to find the optimal layer angles $\pm 51.07^\circ$ with a compliance $c/c_0 = 0.852$. These optimal angles define the initial level-set functions using the method described in Section 6, cf. Figures 12a and 12b in which the color indicates the contour values and every contour represents a toolpath. Starting from this initial design, we solve Equation 32 to obtain the optimal level-set function contours shown in Figure 13a and 13b. As we expect, since $\nu_{max} = 1$, the toolpaths are relatively parallel

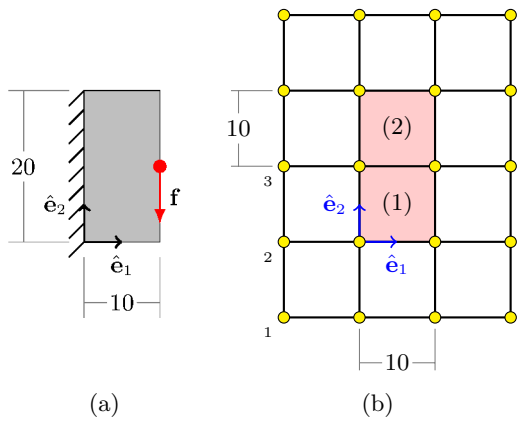

Figure 11: (a) Short cantilever beam. Out of plane thickness is 0.6. (b) Rectangular grid of control points per layer. Dimensions in mm.

and evenly spaced because a fully dense design is stiffer. The compliance for this solution is $c/c_0 = 0.823$, which is stiffer than the initial design.

We form a continuous toolpath for every layer by solving the TSP described in Section 7, cf. Figure 13b and 13d. As expected, the toolpaths are zigzags. We also added an extra connection to link the bottom and top layers. For the bottom layer (cf. Figure 13c), the starting point is the blue triangle and the end point is the blue circle. For the top layer (cf. Figure 13d), the starting point is the red triangle and the end point is the red circle. Figure 13e shows the juxtaposed toolpaths. Notice that the start point of the top layer is above the end point of the bottom layer. This path forms the G-code that controls the AM printer.

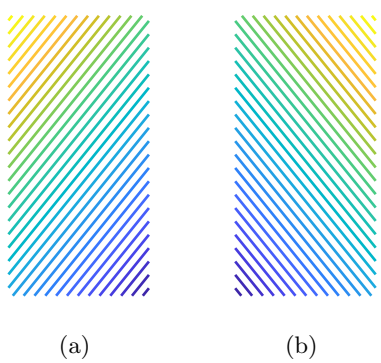

Figure 12: Initial level-set functions for the 2 layer short cantilever problem $\alpha_i = \pm 51.07^\circ$.

We solve the same problem for different volume fraction constraints. Table 1 and Figures 14-16 summarize and illustrate our results. As expected, the compliance increases as the total volume fraction decreases. If the number of active DIW constraints is large, the number of design iterations (It.) increases. This occurs for large maximum volume fraction designs for which the no-overlap constraint is active and for low maximum volume fraction designs for which the no-sag constraint is active. The designs have similar patterns but different spacings between toolpaths. However, in all cases, toolpaths are closer together at the load region. At the bottom and top of the left edge, the toolpaths tend to be horizontal and closely spaced. At the neutral axis, the toolpaths form a cross structure to carry the shear load. Again as expected, the toolpaths are closer where the stress magnitude is higher.

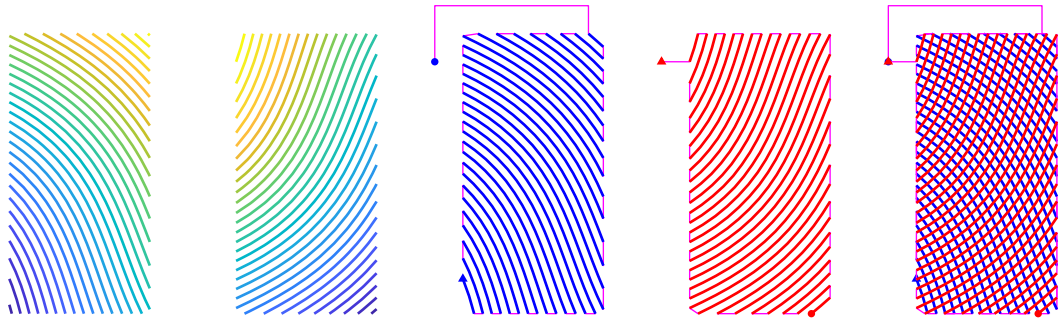

(a) (b) (c) (d) (e)

Figure 13: (a-b) Optimal contours, (c-d) connected toolpaths, and (e) juxtaposed toolpaths for the short cantilever problem with $\nu_{max} = 1.0$.

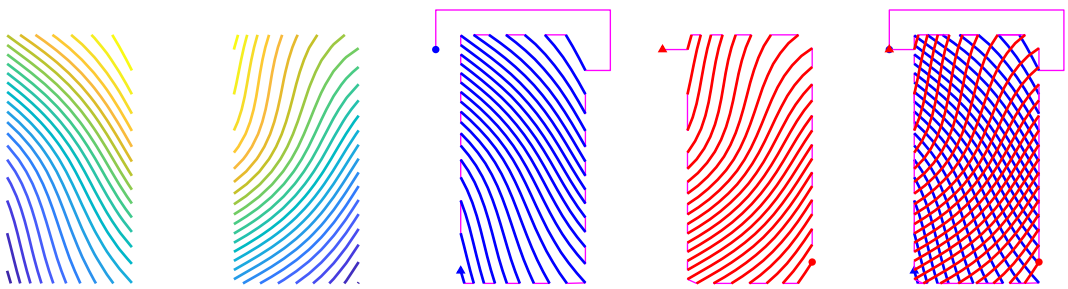

(a) (b) (c) (d) (e)

Figure 14: (a-b) Optimal contours, (c-d) connected toolpaths, and (e) juxtaposed toolpaths for the short cantilever problem with $\nu_{max} = 0.8$.

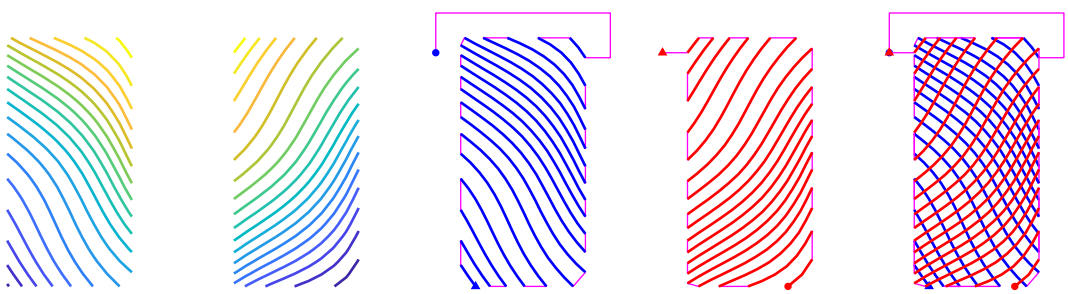

(a) (b) (c) (d) (e)

Figure 15: (a-b) Optimal contours, (c-d) connected toolpaths, and (e) juxtaposed toolpaths for the short cantilever problem with $\nu_{max} = 0.6$.

8.2 Long cantilever beam

In this example we design a 4 layer cantilever beam with dimensions shown in Figure 17 and subject to the line load $\mathbf{f} = -1\,\mathrm{kN/mm}\,\hat{\mathbf{e}}_2$. The finite element mesh has 3200 elements of size $1\,\mathrm{mm} \times 1\,\mathrm{mm} \times 0.3\,\mathrm{mm}$.

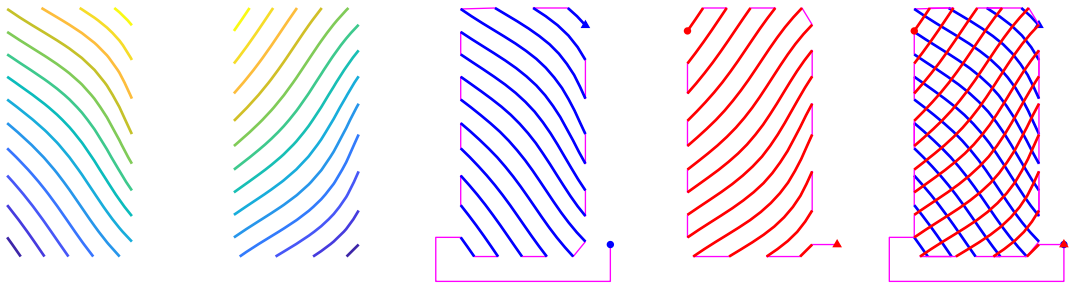

(a) (b) (c) (d) (e)

Figure 16: (a-b) Optimal contours, (c-d) connected toolpaths, and (e) juxtaposed toolpaths for the short cantilever problem with $\nu_{max} = 0.4$.

Table 1: Optimal short beam

ν_{max}	c/c_0	It.
1.00	0.82326	86
0.90	0.84727	50
0.80	0.92063	49
0.70	1.07301	30
0.60	1.09130	31
0.50	1.28922	59
0.40	1.80676	84

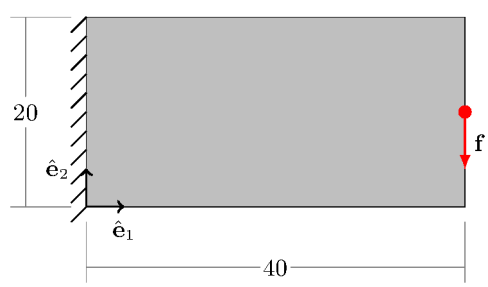

Figure 17: Long cantilever beam. Out of plane thickness is 1.2. Dimensions in mm.

We find the optimal designs for $\nu_{max} = 0.7$ and 5 different stacking sequences: ABCD, ABCA, ABCB, ABAC, and ABAB, where each letter represents an independent layer of the stack. Each layer level-set is defined by a 4×2 B-surface patch totalling $7 \times 5 = 35$ design parameters per layer, so the 5 stacking sequences respectively have 140, 105, 105, and 70 design parameters. In Table 2, we denote the compliances and the number of design iterations for each sequence. We solve the problem for two convergence tolerances $\epsilon_{\text{tol}} = 10^{-3}$ and 10^{-4}. Obviously, the optimizer requires more iterations to satisfy the smaller ϵ_{tol}.

The optimizer is not able to find a feasible solution for the sequence ABCA due to the conflict between the no-sag constraint and the stack pattern. Indeed, the toolpaths of adjacent layers make crossed patterns. Consequently, the top and bottom layers should make a crossed pattern, which is not possible since they are both layer A.

The optimal designs for the different stack sequences have similar patterns as we see in Figures 18 and 19. However, notice that the toolpaths in the uppermost layer of the ABCD design are farther apart compared

to the other layers because it does not serve as a support layer, i.e., the no-sag constraint is not enforced, cf. Figure 18d. Nonetheless, the difference of compliance with the other patterns is less than 2 percent.

Table 2: Optimal long cantilever beam $\nu_{max} = 0.7$.

ϵ_{tol}	10^{-3}		10^{-4}	
Stack	c/c_0	It.	c/c_0	It.
ABCD	1.239509726230	41	1.2371279224296	26
ABCA	-	-	-	-
ABCB	1.254951444685	28	1.2450820886532	34
ABAC	1.251251513357	36	1.2444279586987	56
ABAB	1.246374325178	104	1.2403429915313	66

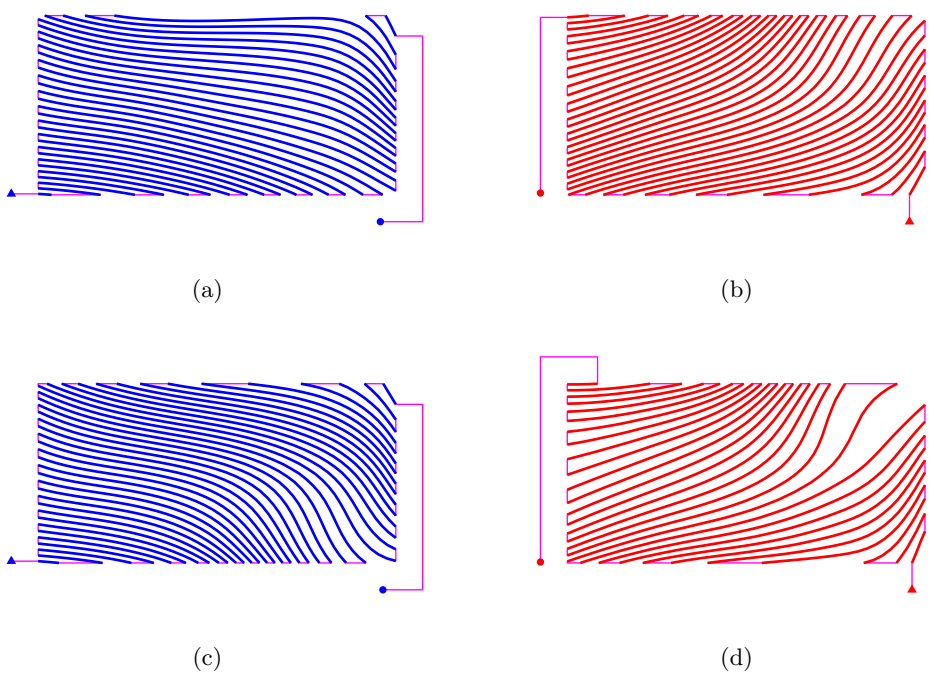

Figure 18: Optimal continuous toolpath for layers (a) A, (b) B, (c) C, and (d) D of the long cantilever beam problem with stack sequence ABCD.

8.3 MBB beam

Our next example is a Messerschmitt-Bölkow-Blohm (MBB) beam with dimensions shown in Figure 20. The beam is made of $n_l = 50$ layers with an ABAB...AB stacking sequence and is subjected to line load $\mathbf{f} = -10\,\text{N/mm}\,\hat{\mathbf{e}}_2$ located at the top center. We discretize the domain with 15000 finite elements of size $1\,\text{mm} \times 1\,\text{mm} \times 0.3\,\text{mm}$. The level-set functions use a 6×1 array of $10\,\text{mm} \times 5\,\text{mm}$ B-surface patches for each layer which yields a total of $72 = 9 \times 4 \times 2$ design parameters. Optimal designs for three total volume fraction limits $\nu_{max} = 1$, 0.8 and 0.6 are obtained, cf. Figure 21.

We printed, tested and compared our designs with $\pm 45^\circ$ designs that have the same volume fractions. The DIW process deposits material continuously, so some regions adjacent to the beam boundary were not modeled in the computations, e.g., the toolpath 'connectors' which are the magenta lines in Figure 21.

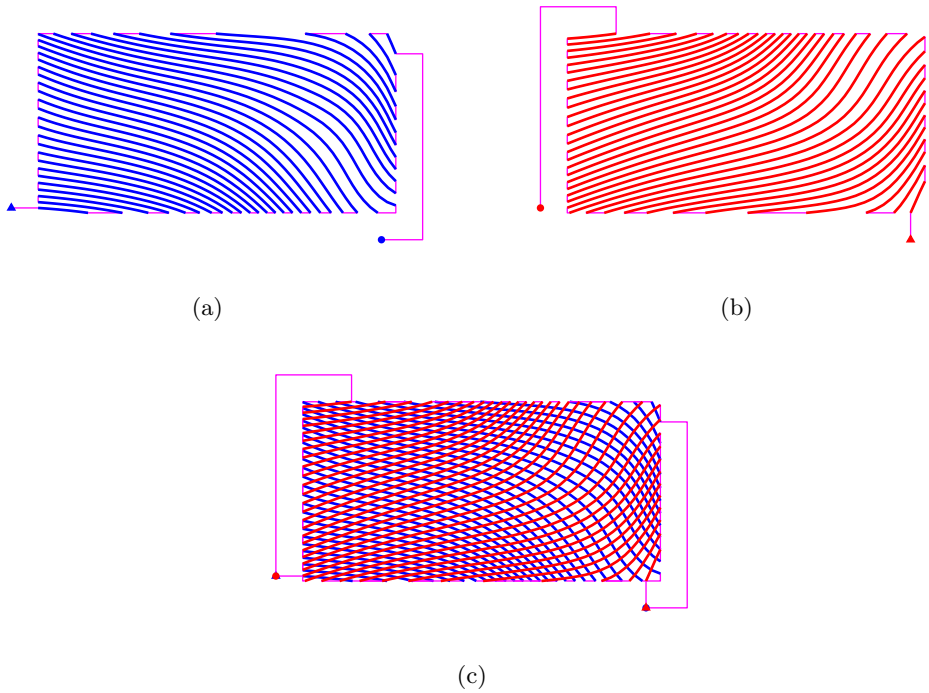

Figure 19: Optimal continuous toolpath for layer (a) A, (b) B, and (c) juxtaposed toolpaths of the cantilever beam problem with stack sequence ABAB.

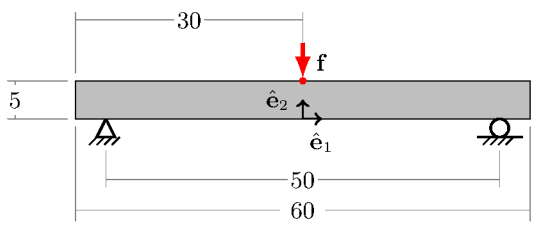

Figure 20: MBB beam problem. Out of plane thickness is 15. All dimensions in mm.

Ultimately, these toolpath connectors should be trimmed in a post substractive manufacturing process. We fabricated three specimens for each sample and performed the three-point bending test according to ASTM D790 specifications. Figure 22 shows the load-deflection curves of these tests in which the straight lines correspond to the simulated finite element responses (square markers are the results c in Table 3). We normalize the load with the mass of each specimen, fit each curve to a cubic polynomial, and then obtain the average curve by averaging the coefficients. To quatify the error between the numerically predicted c and the experimentally measured c^e compliance, we compute the relative error $e = |c - c^e|/c^e 100\%$ under the same load, cf. Table 3. The experimental specimens are more compliant than the numerical prediction, however as we see in Figure 22, for large loads they become stiffer. We attribute the discrepancy to the inaccuracy of the finite element approximation which is known to be too stiff but more so to the material model, cf. Appendix D. As we predict, the optimal designs have lower compliance and as an added benefit a larger failure load compared with the $\pm 45^\circ$ specimens. However, we also observe a counter-intuitive result that the optimized fabricated designs with limit $\nu_{max} = 0.8$ are stiffer than the ones with limit $\nu_{max} = 1$. Our computations predict the opposite. We conjecture that the compactness of the material and volumetric changes in the curing process at large volume fractions, result in higher residual internal stresses which reduce the stiffness and strength. Errors are also attributed to the toolpath that are not trimmed for the experiment but not

modeled in the computation. More data and different volume fraction limits are needed to corroborate this counter-intuitive behavior.

Table 3: Compliance of the MBB beam designs.

Design	ν_{max}	c 10^{-2}[kN mm]	c^e 10^{-2}[kN mm]	e %
Optimized	1	5.2987	6.087	13.0
Optimized	0.8	5.6182	5.786	2.9
Optimized	0.6	6.7839	7.854	13.6
±45°	1	7.3757	10.879	32.2
±45°	0.8	9.2197	12.980	29.0
±45°	0.6	12.2935	13.362	8.0

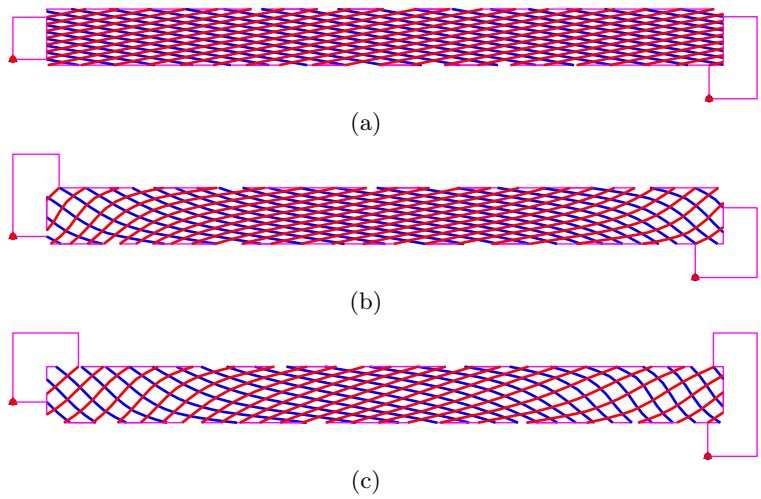

Figure 21: Juxtaposed toolpaths for layers A and B of the MBB problem with (a) $\nu_{max} = 1$, (b) $\nu_{max} = 0.8$, and (c) $\nu_{max} = 0.6$

8.4 Two-hole clevis plate

We next solve the two-hole clevis plate problem illustrated in Figure 23. In the right and left hole, we apply tractions $\mathbf{f} = (100-4(15-x_2)^2)\text{kN/mm}^2\,\hat{\mathbf{e}}_1$ and $-\mathbf{f}$. The plate is made of $n_l = 12$ layers with an ABAB...AB stacking sequence. To model the level-set functions, we use a 6×3 array of $10\,\text{mm} \times 10\,\text{mm}$ B-surface patches for each layer which yields a total of $108 = 9 \times 6 \times 2$ design parameters. The finite element mesh contains 17424 elements. The total volume fraction limit is $\nu_{max} = 0.7$. In Figure 24a, we show the contours of the level-set function for Layer A over the rectangular domain. The total length of the continuous layer A toolpath generated by the TSP is 1821 mm (cf. Figure 24c), which is 8% shorter than the one obtained by the zigzag method (cf. Figure 24b). If the parts have larger holes, the TSP solution will have more significant improvements because the toolpath will avoid the large connections that cross the holes. Also, in the cases where the DIW process continuously deposits material, the TSP solution does not fill the holes which conserves material and reduces post subtractive manufacturing operations. We show the continuous toolpath for layer B in Figure 25a and the continuous juxtaposed toolpaths in Figure 25b. Paths are closer in the load path regions, i.e., the lower and upper regions between the holes; the toolpaths also tend to be horizontal to carry the tensile load in these regions.

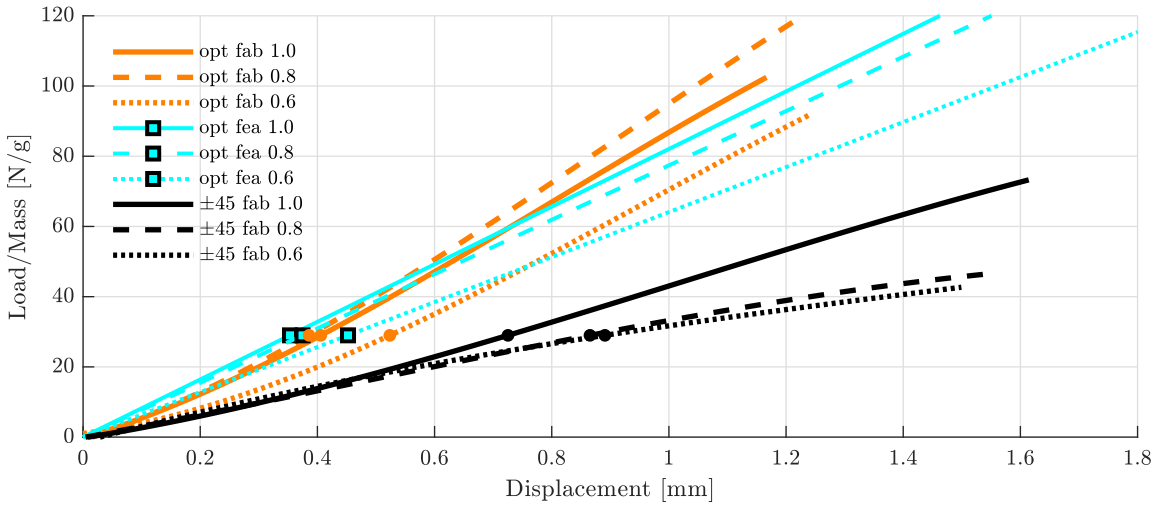

Figure 22: Load-deflection curves of the MBB optimal designs fabricated, optimal design finite element prediction, and ±45° control designs fabricated with $\nu_{max} = 1$, 0.8, and 0.6.

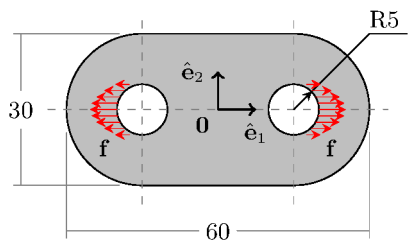

Figure 23: Two holes plate problem. Out of plane thickness is 3.6. All dimensions in mm.

We validate the optimal design by printing the structure shown in Figure 26. There is no overlap of the toolpaths and the material is well supported by the lower layers so no noticeable sagging is present. The abrupt directional changes in the toolpath outside the clevis domain do not matter because they should be removed. What does matter is the fact that the DIW process deposits material continuously and that it satisfies the fabrication constraints inside the clevis domain. We tested and compared this optimal design to ±45° and 0°/90° designs. We perform a modified tensile test where two pins are inserted into the holes and forces are applied to the pins. All samples were measured at ambient temperature at a strain rate of 0.02 mm/min using a Model 1332 Instron machine. Since the masses of the fabricated specimens differ ($m_{opt} = 7.0939$ g, $m_{\pm 45} = 7.9976$ g, $m_{0/90} = 8.3547$ g), we show the load per unit mass vs. displacement curves in Figure 27. As we expected, the optimal design has the lowest compliance per unit mass. Additionally, the optimal design has a higher failure load per unit mass than the other designs. A more detailed description of this experimental validation can be found in [60].

8.5 Five-hole plate

In this example, we solve a five-hole plate design problem with applied forces and dimensions as shown in Figure 28. The holes are squares with sides lengths of 6 mm, the boundary of the center hole is fixed, and the line loads $\mathbf{f}_a = (-\hat{\mathbf{e}}_1 + \hat{\mathbf{e}}_2)$ kN/mm, $\mathbf{f}_b = (-\hat{\mathbf{e}}_1 - \hat{\mathbf{e}}_2)$ kN/mm, $\mathbf{f}_c = (\hat{\mathbf{e}}_1 - \hat{\mathbf{e}}_2)$ kN/mm and $\mathbf{f}_d = (\hat{\mathbf{e}}_1 + \hat{\mathbf{e}}_2)$ kN/mm are applied at the four corners. The plate has 12 layers with an ABAB...AB stacking sequence. To model the level-set functions, we use a 4×4 array of 10 mm × 10 mm B-surface patches for each layer which yields a total of $98 = 7 \times 7 \times 2$ design parameters. The finite element mesh contains 19200 elements of

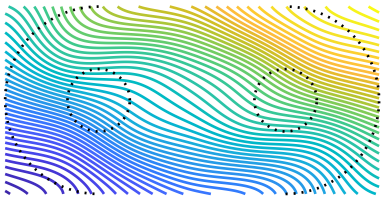

(a)

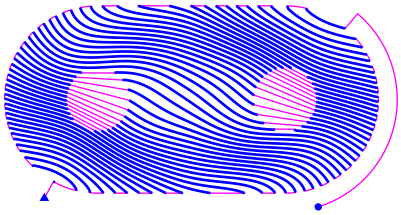

(b)

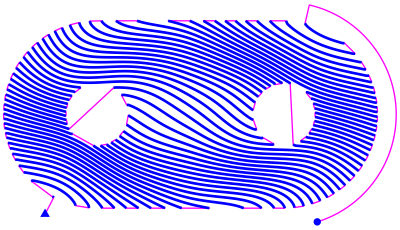

(c)

Figure 24: Contours of level-set function over (a) rectangular domain. (b) Zigzag linking method, and (c) TSP continuous toolpath solution for the layer A of the two-hole clevis plate problem.

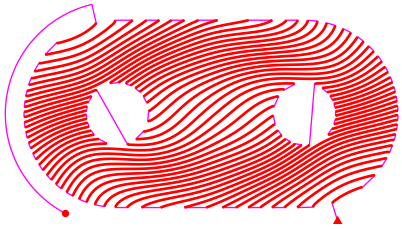

(a)

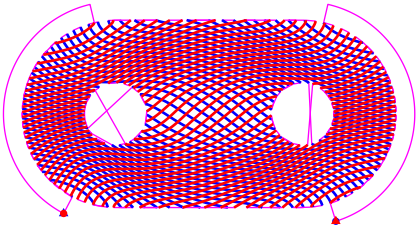

(b)

Figure 25: (a) TSP continuous toolpath for layer B, and (b) juxtaposed toolpaths for layers A and B for the two-hole clevis plate problem.

Figure 26: Fabricated optimal design for the two-hole clevis plate problem.

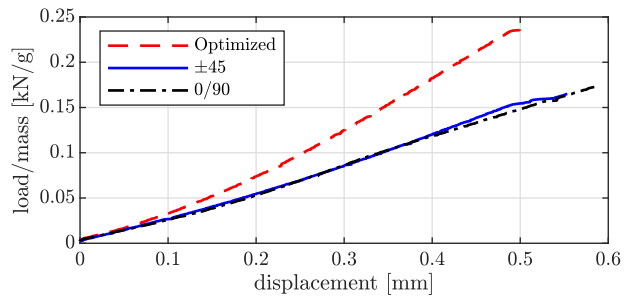

Figure 27: Load per unit mass vs. displacement curves of the two-hole clevis plate optimal design compared with ±45° and 0°/90° designs.

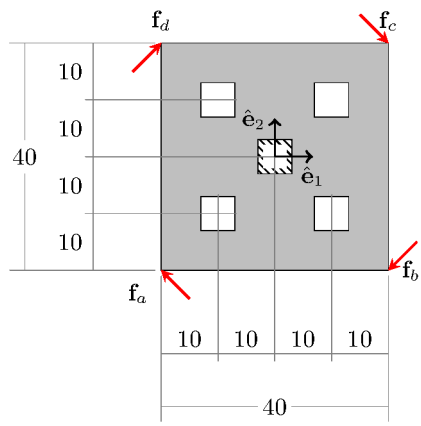

Figure 28: Five hole plate problem. Out of plane thickness is 3.6. All dimensions in mm.

size 1 mm × 1 mm × 0.3 mm and the volume fraction limit is $\nu_{max} = 0.7$. In Figure 29b, we show the TSP generated toolpath for layer A; its length is 1804 mm, which is 8% shorter than the one obtained by the zigzag method (cf. Figure 29a). In Figure 30, we show the layer B toolpath and the juxtaposed toolpaths. As we expected, paths are closer in the regions around the central hole which carries the brunt of the load.

If we modify the TSP distance definitions, the toolpaths vary accordingly. For instance, to avoid crossing the holes, we penalize the distance of non-adjacent cities that are on the hole boundaries. We impose $c_{j,k} = d_\infty$ if $\mathbf{x}_j \in \partial P_i^{Hr}$, $\mathbf{x}_k \in \partial P_i^{Hr}$ and cities $< j >$ and $< k >$ are not adjacent. In Figure 31, we show the toolpath of this modified TSP. As expected, the toolpaths avoid crossing the holes, however, extra connections between non-adjacent cities at the external boundary appear. We fabricate the optimal design shown in Figure 32.

9 Conclusions

This paper demonstrates a method for optimizing FRC structures fabricated by AM that accommodates manufacturability constraints of the DIW process, maintains computational efficiency, and guarantees optimality.

The toolpaths of each layer are defined by the contours of a level-set function. With this representation, the toolpaths are continuous and defined with a small number of design variables over a fixed grid that is independent of the finite element mesh used for structural analysis. The toolpath spacing, angle, and curvature are defined from the level-set function. In this way, it is easy to impose DIW manufacturing constraints related to overlap, sag, radius of curvature, and toolpath continuity. For each layer, these local constraints are enforced globally, using a ramp function, resulting in a small number of constraints.

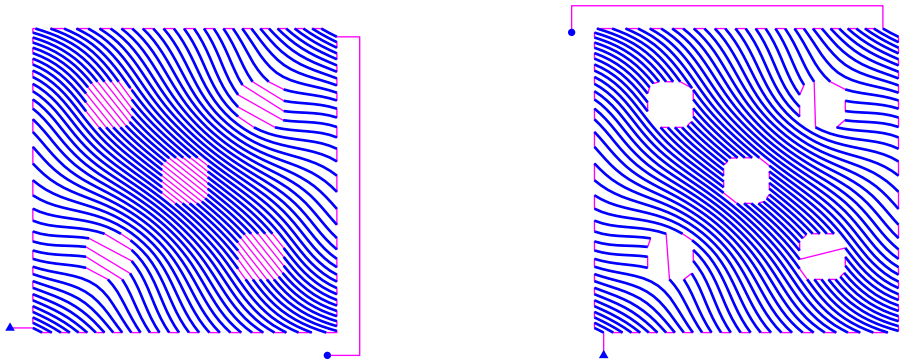

(a) (b)

Figure 29: Continuous toolpath obtained with (a) zigzag method, and (b) TSP solution for layer A of the 5 hole-plate problem.

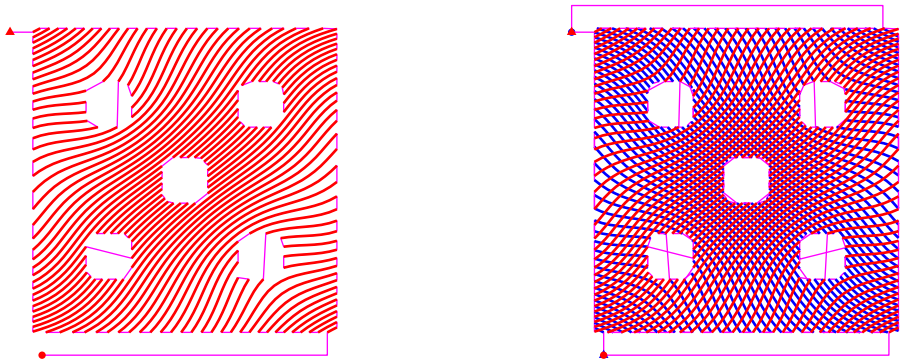

(a) (b)

Figure 30: (a) TSP continuous toolpath for layer B, and (b) juxtaposed toolpaths for layers A and B for the five-hole plate problem.

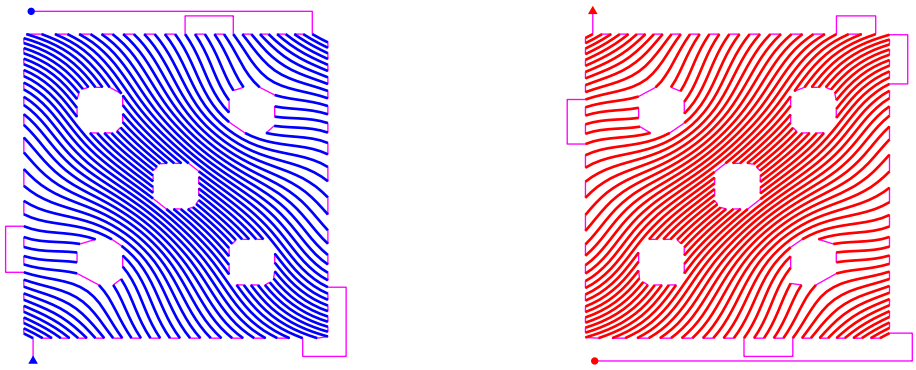

(a) (b)

Figure 31: Modified TSP solution toolpath (a) layer A, and (b) layer B for the five-hole plate problem.

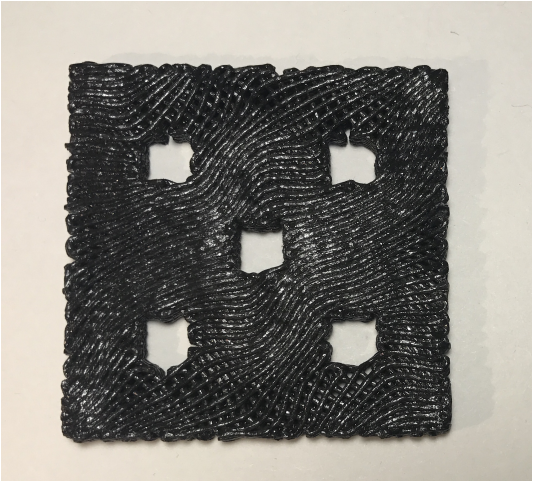

Figure 32: Fabricated optimal design for the five-hole plate problem.

The toolpaths also determine the orientation of the reinforcement fibers and their volume fraction and hence the structural response of the composite structure. We use the finite element method to compute the structure's mass and compliance and their design sensitivities. These computations are combined with nonlinear programming to efficiently update the design parameters and find locally optimal designs.

The optimized toolpaths start and finish at the boundary of each layer. To minimize manufacturing cost, we formulate and solve a TSP to obtain the shortest continuous toolpath for each layer. This continuous toolpath is subsequently used to generate the G-code for fabrication.

We validate our approach by designing minimum compliance composite structures, some of which we fabricate. We further validate some of the optimized designs by experiment and compare them to nonoptimized designs.

For future work, the authors will extend this implementation to optimize other structural properties like strength, buckling, etc. The material model also needs to be fully studied and improved. We also want to explore the possibility of working on curved rather than plane surfaces and implement this approach for other AM, ATP, and AFP technologies. Perhaps this approach can be used to design components fabricated via Selective Laser Melt (SLM) processes. For this we would need a model that relates the laser trajectory to the material's anisotropic material properties. Finally, we want to integrate this approach with TO to simultaneously optimize the toolpaths and the domain.

Acknowledgment

Portions of this work were performed under the auspices of the U.S. Department of Energy by Lawrence Livermore National Laboratory (LLNL) under Contract DE-AC52-07NA27344, cf. ref number LLNL-CONF-717659. We would also like to thank Professor Karthekeyan Chandrasekaran at the University of Illinois at Urbana-Champaign (UIUC) for providing us guidance about the TSP formulation and solver, Yuta Saito and Professor John Lambros at UIUC for performing experimental work on the two-hole clevis plate specimens, and Swetha Chandrasekaran at LLNL for assisting with mechanical tests on the MBB beams.

References

References

[1] H. Ghiasi, K. Fayazbakhsh, D. Pasini, L. Lessard, Optimum stacking sequence design of composite materials part i: Constant stiffness design, Composite Structures 90 (2009) 1 – 11.

[2] G. Gonzalez Lozano, A. Tiwari, C. Turner, S. Astwood, A review on design for manufacture of variable stiffness composite laminates, Proceedings of the Institution of Mechanical Engineers, Part B: Journal of Engineering Manufacture 230 (6) (2016) 981–992.

[3] H. Ghiasi, K. Fayazbakhsh, D. Pasini, L. Lessard, Optimum stacking sequence design of composite materials part ii: Variable stiffness design, Composite Structures 93 (1) (2010) 1 – 13.

[4] Z. Gürdal, R. T. Haftka, P. Hajela, Design and optimization of laminated composite materials, John Wiley & Sons, 1999.

[5] R. T. Haftka, Z. Gürdal, Elements of structural optimization, Vol. 11, Springer Netherlands, 1992.

[6] D. Brackett, I. Ashcroft, R. Hague, Topology optimization for additive manufacturing, in: Proceedings of the solid freeform fabrication symposium, Austin, TX, Vol. 1, S, 2011, pp. 348–362.

[7] A. T. Gaynor, J. K. Guest, Topology optimization for additive manufacturing: considering maximum overhang constraint, in: 15th AIAA/ISSMO multidisciplinary analysis and optimization conference, 2014, pp. 16–20.

[8] O. Sigmund, J. Petersson, Numerical instabilities in topology optimization: A survey on procedures dealing with checkerboards, mesh-dependencies and local minima, Structural optimization 16 (1) (1998) 68–75.

[9] T. E. Bruns, D. A. Tortorelli, Topology optimization of non-linear elastic structures and compliant mechanisms, Computer Methods in Applied Mechanics and Engineering 190 (26) (2001) 3443–3459.

[10] T. A. Poulsen, A new scheme for imposing a minimum length scale in topology optimization, International Journal for Numerical Methods in Engineering 57 (6) (2003) 741–760.

[11] J. K. Guest, J. H. Prévost, T. Belytschko, Achieving minimum length scale in topology optimization using nodal design variables and projection functions, International journal for numerical methods in engineering 61 (2) (2004) 238–254.

[12] J. K. Guest, Imposing maximum length scale in topology optimization, Structural and Multidisciplinary Optimization 37 (5) (2009) 463–473.

[13] C. Xu, W. Chai, Y. Huang, R. R. Markwald, Scaffold-free inkjet printing of three-dimensional zigzag cellular tubes, Biotechnology and bioengineering 109 (12) (2012) 3152–3160.

[14] M. Langelaar, Topology optimization of 3D self-supporting structures for additive manufacturing, Additive Manufacturing 12 (2016) 60 – 70.

[15] M. Langelaar, An additive manufacturing filter for topology optimization of print-ready designs, Structural and Multidisciplinary Optimization 55 (3) (2017) 871–883.

[16] A. Hussein, L. Hao, C. Yan, R. Everson, P. Young, Advanced lattice support structures for metal additive manufacturing, Journal of Materials Processing Technology 213 (7) (2013) 1019–1026.

[17] J.-P. Järvinen, V. Matilainen, X. Li, H. Piili, A. Salminen, I. Mäkelä, O. Nyrhilä, Characterization of effect of support structures in laser additive manufacturing of stainless steel, Physics Procedia 56 (2014) 72 – 81, 8th International Conference on Laser Assisted Net Shape Engineering LANE 2014.

[18] P. Zhang, J. Liu, A. C. To, Role of anisotropic properties on topology optimization of additive manufactured load bearing structures, Scripta Materialia.

[19] M. K. Thompson, G. Moroni, T. Vaneker, G. Fadel, R. I. Campbell, I. Gibson, A. Bernard, J. Schulz, P. Graf, B. Ahuja, et al., Design for additive manufacturing: Trends, opportunities, considerations, and constraints, CIRP Annals-Manufacturing Technology 65 (2) (2016) 737–760.

[20] M. M. Abdalla, Z. Gürdal, Structural design using optimality based cellular automata, in: Proceedings of 43rd AIAA/ASME/ASCE/AHS/ASC Structures, Structural Dynamics, and Materials Conference, 2002, p. 1676.

[21] M. M. Abdalla, S. Setoodeh, Z. Gürdal, Design of variable stiffness composite panels for maximum fundamental frequency using lamination parameters, Composite Structures 81 (2) (2007) 283 – 291.

[22] S. Setoodeh, M. M. Abdalla, S. T. IJsselmuiden, Z. Gürdal, Design of variable–stiffness composite panels for maximum buckling load, Composite Structures 87 (1) (2009) 109 – 117.

[23] S. Setoodeh, A. W. Blom, M. M. Abdalla, Z. Gürdal, Generating curvilinear fiber paths from lamination parameters distribution, in: Proceedings of the 47th AIAA/ASME/ASCE/AHS/ASC Structures, Structural Dynamics and Materials (SDM) Conference. Newport, RI, 2006, p. 1875.

[24] S. Setoodeh, Z. Gürdal, L. T. Watson, Design of variable–stiffness composite layers using cellular automata, Computer Methods in Applied Mechanics and Engineering 195 (9) (2006) 836 – 851.

[25] A. W. Blom, M. M. Abdalla, Z. Gürdal, Optimization of course locations in fiber–placed panels for general fiber angle distributions, Composites Science and Technology 70 (4) (2010) 564–570.

[26] C. Kiyono, E. Silva, J. Reddy, A novel fiber optimization method based on normal distribution function with continuously varying fiber path, Composite Structures 160 (2017) 503–515.

[27] R. Olmedo, Z. Gürdal, Buckling response of laminates with spatially varying fiber orientations, in: AIAA/ASME/ASCE/AHS/ASC 34th Structures, Structural Dynamics, and Materials Conference, 1993, pp. 2261–2269.

[28] S. Nagendra, S. Kodiyalam, J. Davis, V. Parthasarathy, Optimization of tow fiber paths for composite design, in: AIAA/ASME/ASCE/AHS/ASC 36th Structures, Structural Dynamics and Materials Conference, 1995, pp. 2261–2269.

[29] B. F. Tatting, Analysis and design of variable stiffness composite cylinders, Ph.D. thesis, Ph. D. Thesis, Virginia Polytechnic Institute and State University, Blacksburg, Virginia, USA (1998).

[30] L. Parnas, S. Oral, Ü. Ceyhan, Optimum design of composite structures with curved fiber courses, Composites science and technology 63 (7) (2003) 1071–1082.

[31] A. W. Blom, P. B. Stickler, Z. Gürdal, Design and manufacture of a variable–stiffness cylindrical shell, in: Proceedings of the SAMPE Europe 30th International Conference, SAMPE Europe, 2009, pp. 1–8.

[32] A. W. Blom, B. F. Tatting, J. M. Hol, Z. Gürdal, Fiber path definitions for elastically tailored conical shells, Composites part B: engineering 40 (1) (2009) 77–84.

[33] K. Dems, J. Wiśniewski, Optimal design of fiber-reinforced composite disks, Journal of Theoretical and Applied Mechanics 47 (3) (2009) 515–535.

[34] F. Luraghi, Surrogate-based shape optimization of fiber paths in tow-steered laminates for maximum buckling load, in: F. AJM (Ed.), 16th international conference on composite structures, University of Porto, 2011, pp. 28–30.

[35] Z. Zamani, H. Haddadpour, M.-R. Ghazavi, Curvilinear fiber optimization tools for design thin walled beams, Thin-Walled Structures 49 (3) (2011) 448–454.

[36] H. Haddadpour, Z. Zamani, Curvilinear fiber optimization tools for aeroelastic design of composite wings, Journal of Fluids and Structures 33 (2012) 180–190.

[37] Z. Wu, P. M. Weaver, G. Raju, B. C. Kim, Buckling analysis and optimisation of variable angle tow composite plates, Thin–walled structures 60 (2012) 163–172.

[38] B. F. Tatting, Z. Gürdal, D. Jegley, Design and manufacture of elastically tailored tow placed plates, Tech. Rep. CR-211919, NASA (August 2002).

[39] C. Waldhart, Analysis of tow-placed, variable-stiffness laminates, Master's thesis, Virginia Polytechnic Institute and State University (1996).

[40] C. Waldhart, Z. Gürdal, C. Ribbens, Analysis of tow placed, parallel fiber, variable stiffness laminates, in: 37th Structure, Structural Dynamics and Materials Conference, 1996, p. 1569.

[41] S. T. IJsselmuiden, Optimal design of variable stiffness composite structures using lamination parameters, Ph.D. thesis, TUDelft (October 2011).

[42] J. M. Van Campen, C. Kassapoglou, Z. Gürdal, Generating realistic laminate fiber angle distributions for optimal variable stiffness laminates, Composites Part B: Engineering 43 (2) (2012) 354 – 360.

[43] C. Brampton, K. Wu, H. Kim, New optimization method for steered fiber composites using the level set method, Structural and Multidisciplinary Optimization 52 (3) (2015) 493–505.

[44] J. A. Sethian, Level set methods and fast marching methods: evolving interfaces in computational geometry, fluid mechanics, computer vision, and materials science, Vol. 3, Cambridge university press, 1999.

[45] J. H. Luo, H. C. Gea, Optimal orientation of orthotropic materials using an energy based method, Structural optimization 15 (3) (1998) 230–236.

[46] J. Roberge, J. Norato, Computational design of curvilinear bone scaffolds fabricated via direct ink writing, Computer-Aided Design.

[47] J. Liu, H. Yu, Concurrent deposition path planning and structural topology optimization for additive manufacturing, Rapid Prototyping Journal 23 (5) (2017) 930–942.

[48] J. Liu, A. C. To, Deposition path planning-integrated structural topology optimization for 3d additive manufacturing subject to self-support constraint, Computer-Aided Design 91 (2017) 27–45.

[49] J. P. Lewicki, J. N. Rodriguez, C. Zhu, M. A. Worsley, A. S. Wu, Y. Kanarska, J. D. Horn, E. B. Duoss, J. M. Ortega, W. Elmer, et al., 3d-printing of meso-structurally ordered carbon fiber/polymer composites with unprecedented orthotropic physical properties, Scientific Reports 7 (2017) 43401.

[50] N. J. Zabusky, E. A. Overman, Regularization of contour dynamical algorithms. i. tangential regularization, Journal of Computational Physics 52 (2) (1983) 351 – 373.

[51] S. Osher, J. A. Sethian, Fronts propagating with curvature-dependent speed: Algorithms based on Hamilton-Jacobi formulations, Journal of Computational Physics 79 (1) (1988) 12 – 49.

[52] S. Amstutz, A. A. Novotny, E. A. de Souza Neto, Topological derivative-based topology optimization of structures subject to Drucker–Prager stress constraints, Computer Methods in Applied Mechanics and Engineering 233 (2012) 123 – 136.

[53] C. Le, J. Norato, T. Bruns, C. Ha, D. Tortorelli, Stress–based topology optimization for continua, Structural and Multidisciplinary Optimization 41 (4) (2010) 605–620.

[54] D. A. Tortorelli, P. Michaleris, Design sensitivity analysis: Overview and review, Inverse Problems in Engineering 1 (1) (1994) 71–105.

[55] M. P. Bendsøe, O. Sigmund, Topology optimization by distribution of isotropic material, Springer, 2004.

[56] A. Wächter, L. T. Biegler, On the implementation of a primal-dual interior point filter line search algorithm for large-scale nonlinear programming, Mathematical Programming 106 (1) (2006) 25–57.

[57] Z. Lin, J. Fu, H. Shen, W. Gan, S. Yue, Tool path generation for multi-axis freeform surface finishing with the LKH TSP solver, Computer-Aided Design 69 (2015) 51–61.

[58] D. L. Applegate, R. E. Bixby, V. Chvatal, W. J. Cook, The traveling salesman problem: a computational study, Princeton university press, 2011.

[59] M. Puso, B. N. Maker, R. M. Ferencz, J. O. Hallquist, Nike3d: a nonlinear, implicit, three-dimensional finite element code for solid and structural mechanics, Users Manual.

[60] Y. Saito, F. Fernandez, D. A. Tortorelli, W. S. Compel, J. P. Lewicki, J. Lambros, Experimental validation of an additively manufactured stiffness-optimized short-fiber reinforced composite clevis joint, Experimental Mechanics (2019) 1–11.

Appendices

A B-surface

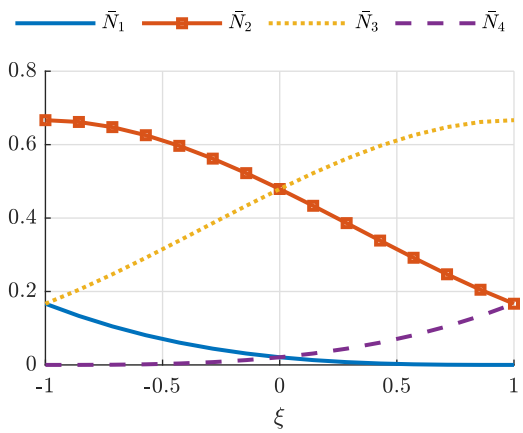

Figure A.1: Cubic B-spline shape functions.

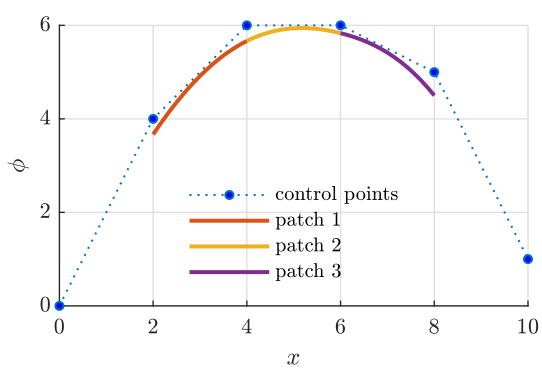

Figure A.2: B-spline curve (x, ϕ) with grid of control point coordinates $\bar{\mathbf{X}} = [0, 2, 4, 6, 8, 10]^\top$ and vector of height parameters $\mathbf{d} = [0, 4, 6, 6, 5, 1]^\top$.

In one dimension, the uniform cubic B-spline shape functions are defined as

$$
\begin{aligned}
\bar{N}_1(\xi) &= \frac{1}{48}(1 - 3\xi + 3\xi^2 - \xi^3)\,, \\
\bar{N}_2(\xi) &= \frac{1}{48}(23 - 15\xi - 3\xi^2 + 3\xi^3)\,, \\
\bar{N}_3(\xi) &= \frac{1}{48}(23 + 15\xi - 3\xi^2 - 3\xi^3)\,, \\
\bar{N}_4(\xi) &= \frac{1}{48}(1 + 3\xi + 3\xi^2 + \xi^3)\,,
\end{aligned}
\tag{A.1}
$$

where $\xi \in [-1, 1]$. A B-spline $(x(\xi), \phi(\xi))$ is composed by segments (or patches) such that $x(\xi) = \bar{\mathbf{X}}_i^\top \bar{\mathbf{N}}(\boldsymbol{\xi})$ and $\phi(\xi) = \mathbf{d}_i^\top \bar{\mathbf{N}}(\boldsymbol{\xi})$ where $\bar{\mathbf{X}}_i$ is the 4×1 local vector of control point coordinates and $\mathbf{d}_i$ is the 4×1 local vector of height parameters for the patch i, cf. Figure A.2.

For two-dimensions, the shape functions for uniform bi-cubic B-surface shape functions over the $[-1, 1]^2$ domain are obtained from the outer product of the B-spline functions, i.e.,

$$
\hat{\mathbf{N}}(\boldsymbol{\xi}) = [\bar{N}_1(\xi_1)\bar{N}_1(\xi_2), \bar{N}_1(\xi_1)\bar{N}_2(\xi_2), \bar{N}_1(\xi_1)\bar{N}_3(\xi_2), ..., \bar{N}_4(\xi_1)\bar{N}_4(\xi_2)]^\mathsf{T}\,. \tag{A.2}
$$

For simplicity, we use a rectangular domain with uniform rectangular patches. If we have n_x by n_y patches, there is a total of $(n_x + 3)(n_y + 3)$ control points, e.g., the B-surface in Figure 3 has 4×3 patches with a total of 7×6 control points. Given the physical control grid point coordinates $\hat{\mathbf{X}}_i = [\mathbf{x}_1\ \mathbf{x}_2\ \ldots\ \mathbf{x}_{16}]^\mathsf{T}$ for the patch i, and a position $\mathbf{x} \in \mathbb{R}^2$ in the patch, the level-set function $\phi \in \mathbb{R}$ is defined with an iso-parametric formulation, i.e.,

$$
\phi(\mathbf{x})|_{\mathbf{x}=\hat{\mathbf{X}}_i^\mathsf{T}\hat{\mathbf{N}}(\boldsymbol{\xi})} = \mathbf{d}_i^\mathsf{T}\,\hat{\mathbf{N}}(\boldsymbol{\xi})\,, \tag{A.3}
$$

where $\mathbf{d}_i$ is the 16×1 vector of height parameters for the patch i. Since we use a rectangular domain, the inverse mapping is straight forward

$$
\boldsymbol{\xi} = 2\,\mathrm{diag}\left(\frac{1}{h_x}, \frac{1}{h_y}\right)(\mathbf{x} - \mathbf{x}_c)\,, \tag{A.4}
$$

where $\mathbf{x}_c$ is the center location of the patch and h_x and h_y are the edge lengths of the patches in the $\hat{\mathbf{e}}_1$ and $\hat{\mathbf{e}}_2$ directions, cf. Figure A.3.

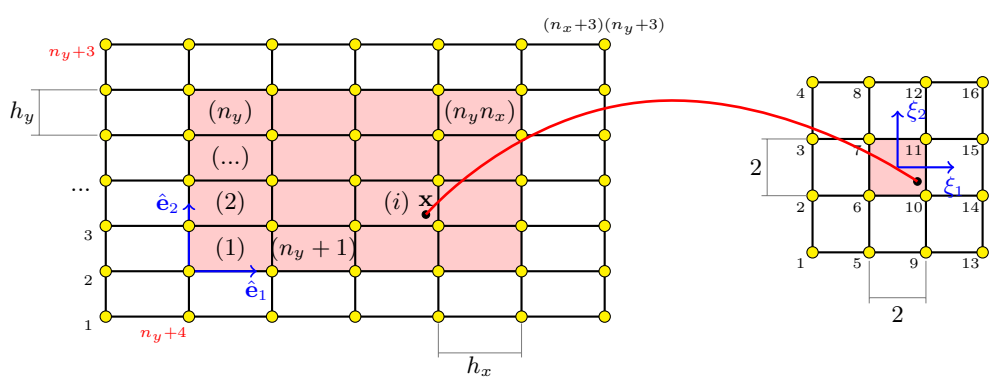

Figure A.3: Rectangular grid of control points in physical coordinates and mapping with respect to the reference coordinate system.

B Composite properties

The material properties used for the examples correspond to a short carbon fiber composite with fiber volume fraction $v_f = 0.062$, fiber length $l_f = 500\,\mu\mathrm{m}$, and fiber diameter $d_f = 0.7\,\mu\mathrm{m}$. The short carbon

fiber composite is modeled as transversely isotropic material where the axis of isotropy is aligned with the fiber direction. We use the composite material with elastic constants $E_L = 7.48\,\text{GPa}$, $E_T = 4.47\,\text{GPa}$, $G_{LT} = 1.7\,\text{GPa}$, $G_{TT} = 1.63\,\text{GPa}$, $\nu_{LT} = 0.33$, $\nu_{TT} = 0.37$, and density $\rho = 1.15\,\text{g/cm}^3$. For the local coordinate system, the fiber direction is defined as the $\hat{\mathbf{e}}_1$ direction. We employ the following Voigt convention for the stress, strain and stiffness

$$[\sigma_1, \sigma_2, \sigma_3, \sigma_4, \sigma_5, \sigma_6] = [\sigma_{xx}, \sigma_{yy}, \sigma_{zz}, \sigma_{xy}, \sigma_{yz}, \sigma_{xz}], \tag{B.1}$$

$$[\epsilon_1, \epsilon_2, \epsilon_3, \epsilon_4, \epsilon_5, \epsilon_6] = [\epsilon_{xx}, \epsilon_{yy}, \epsilon_{zz}, 2\epsilon_{xy}, 2\epsilon_{yz}, 2\epsilon_{xz}], \tag{B.2}$$

$$\begin{bmatrix} \sigma_1 \\ \sigma_2 \\ \sigma_3 \\ \sigma_4 \\ \sigma_5 \\ \sigma_6 \end{bmatrix} = [\mathbb{C}_0] \begin{bmatrix} \epsilon_1 \\ \epsilon_2 \\ \epsilon_3 \\ \epsilon_4 \\ \epsilon_5 \\ \epsilon_6 \end{bmatrix} = \begin{bmatrix} c_{11}^0 & c_{12}^0 & c_{12}^0 & 0 & 0 & 0 \\ c_{12}^0 & c_{22}^0 & c_{23}^0 & 0 & 0 & 0 \\ c_{12}^0 & c_{23}^0 & c_{22}^0 & 0 & 0 & 0 \\ 0 & 0 & 0 & c_{44}^0 & 0 & 0 \\ 0 & 0 & 0 & 0 & c_{55}^0 & 0 \\ 0 & 0 & 0 & 0 & 0 & c_{44}^0 \end{bmatrix} \begin{bmatrix} \epsilon_1 \\ \epsilon_2 \\ \epsilon_3 \\ \epsilon_4 \\ \epsilon_5 \\ \epsilon_6 \end{bmatrix}. \tag{B.3}$$

The relationships between the material constants and the stiffness components for a transversely isotropic material are given by

$$\begin{aligned} \nu_{TL} &= \nu_{LT} \frac{E_T}{E_L} \\ \Delta &= 1 - 2\nu_{LT}\nu_{TL} - \nu_{TT}\nu_{TT} - 2\nu_{LT}\nu_{TT}\nu_{TL} \\ c_{11}^0 &= E_L \frac{(1 - \nu_{TT}^2)}{\Delta} \\ c_{22}^0 &= E_T \frac{(1 - \nu_{LT}\nu_{TL})}{\Delta} \\ c_{12}^0 &= E_T \nu_{LT} \frac{(1 + \nu_{TT})}{\Delta} \\ c_{23}^0 &= E_T \frac{\nu_{TT} + \nu_{TL}\nu_{LT}}{\Delta} \\ c_{44}^0 &= G_{LT} \\ c_{55}^0 &= G_{TT} \end{aligned} . \tag{B.4}$$

C Transformation of the stiffness

The stiffness in the global system is defined via Equation (25) where the rotation matrix is given by

$$\mathbf{R}_z(\alpha) = \begin{bmatrix} \cos(\alpha) & -\sin(\alpha) & 0 \\ \sin(\alpha) & \cos(\alpha) & 0 \\ 0 & 0 & 1 \end{bmatrix}. \tag{C.1}$$

Consistent with our Voigt notation, it can be shown that

$$\mathbf{R_z}(\alpha) \boxtimes \mathbf{R_z}(\alpha) = \begin{bmatrix} \cos^2(\alpha) & \sin^2(\alpha) & 0 & -2\cos(\alpha)\sin(\alpha) & 0 & 0 \\ \sin^2(\alpha) & \cos^2(\alpha) & 0 & 2\cos(\alpha)\sin(\alpha) & 0 & 0 \\ 0 & 0 & 1 & 0 & 0 & 0 \\ \cos(\alpha)\sin(\alpha) & -\cos(\alpha)\sin(\alpha) & 0 & \cos^2(\alpha) - \sin^2(\alpha) & 0 & 0 \\ 0 & 0 & 0 & 0 & \cos(\alpha) & \sin(\alpha) \\ 0 & 0 & 0 & 0 & -\sin(\alpha) & \cos(\alpha) \end{bmatrix}. \tag{C.2}$$

We use the trigonometric functions of multiple angles to reduce the numerical error in the computation

of the rotation tensors and their sensitivities

$$
\begin{aligned}
cs &= \cos(\alpha)\sin(\alpha) &&= \sin(2\alpha)/2\,,\\
c^2 &= \cos^2(\alpha) &&= (1+\cos(2\alpha))/2\,,\\
s^2 &= \sin^2(\alpha) &&= (1-\cos(2\alpha))/2\,,\\
c^4 &= \cos^4(\alpha) &&= (3+4\cos(2\alpha)+\cos(4\alpha))/8\,,\\
s^4 &= \sin^4(\alpha) &&= (3-4\cos(2\alpha)+\cos(4\alpha))/8\,,\\
c^2s^2 &= \cos^2(\alpha)\sin^2(\alpha) &&= (1-\cos(4\alpha))/8\,,\\
c^3s &= \cos^3(\alpha)\sin(\alpha) &&= (2\sin(2\alpha)+\sin(4\alpha))/8\,,\\
cs^3 &= \cos(\alpha)\sin^3(\alpha) &&= (2\sin(2\alpha)-\sin(4\alpha)a)/8\,.
\end{aligned}
\tag{C.3}
$$

In this way the components of the rotated elasticity tensor $\mathbb{C}(\alpha)$, cf. Equation (25), in Voigt notation are

$$
\begin{aligned}
c_{11} &= c^0_{11}c^4 + c^0_{22}s^4 + (2c^0_{12}+4c^0_{44})c^2s^2\,,\\
c_{12} &= c^0_{12}(c^4+s^4) + (c^0_{22}+c^0_{11}-4c^0_{44})c^2s^2\,,\\
c_{13} &= c^0_{12}c^2 + c^0_{23}s^2\,,\\
c_{14} &= (c^0_{11}-c^0_{12}-2c^0_{44})c^3s + (c^0_{12}-c^0_{22}+2c^0_{44})cs^3\,,\\
c_{22} &= c^0_{22}c^4 + c^0_{11}s^4 + (2c^0_{12}+4c^0_{44})c^2s^2\,,\\
c_{23} &= c^0_{23}c^2 + c^0_{12}s^2\,,\\
c_{24} &= (c^0_{11}-c^0_{12}-2c^0_{44})cs^3 + (c^0_{12}-c^0_{22}+2c^0_{44})c^3s\,,\\
c_{33} &= c^0_{22}\,,\\
c_{34} &= (c^0_{12}-c^0_{23})cs\,,\\
c_{44} &= c^0_{44}(c^4-2c^2s^2+s^4) + (c^0_{11}-2c^0_{12}+c^0_{22})c^2s^2\,,\\
c_{55} &= c^0_{55}c^2 + c^0_{44}s^2\,,\\
c_{56} &= (c^0_{44}-c^0_{55})cs\,,\\
c_{66} &= c^0_{44}c^2 + c^0_{55}s^2\,.
\end{aligned}
\tag{C.4}
$$

To evaluate the sensitivity of the stiffness matrix respect to the angle, i.e., $\mathrm{d}\mathbb{C}/\mathrm{d}\alpha$, we define

$$
\begin{aligned}
\mathrm{d}c^4 &= (-2\sin(2\alpha)-\sin(4\alpha))/2\,,\\
\mathrm{d}s^4 &= (2\sin(2\alpha)-\sin(4\alpha))/2\,,\\
\mathrm{d}c^3s &= (\cos(2\alpha)+\cos(4\alpha))/2\,,\\
\mathrm{d}cs^3 &= (\cos(2\alpha)-\cos(4\alpha))/2\,,
\end{aligned}
\tag{C.5}
$$

$$
\begin{aligned}
\mathrm{d}c_{11} &= c^0_{11}\mathrm{d}c^4 + c^0_{22}\mathrm{d}s^4 + (c^0_{12}+2c^0_{44})\sin(4\alpha)\,,\\
\mathrm{d}c_{12} &= c^0_{12}(\mathrm{d}c^4+\mathrm{d}s^4) + (c^0_{22}+c^0_{11}-4c^0_{44})\sin(4\alpha)/2\,,\\
\mathrm{d}c_{13} &= (-c^0_{12}+c^0_{23})\sin(2\alpha)\,,\\
\mathrm{d}c_{14} &= (c^0_{11}-c^0_{12}-2c^0_{44})\mathrm{d}c^3s + (c^0_{12}-c^0_{22}+2c^0_{44})\mathrm{d}cs^3\,,\\
\mathrm{d}c_{22} &= c^0_{22}\mathrm{d}c^4 + c^0_{11}\mathrm{d}s^4 + (c^0_{12}+2c^0_{44})\sin(4\alpha)\,,\\
\mathrm{d}c_{23} &= (-c^0_{23}+c^0_{12})\sin(2\alpha)\,,\\
\mathrm{d}c_{24} &= (c^0_{11}-c^0_{12}-2c^0_{44})\mathrm{d}cs^3 + (c^0_{12}-c^0_{22}+2c^0_{44})\mathrm{d}c^3s\,,\\
\mathrm{d}c_{34} &= (c^0_{12}-c^0_{23})\cos(2\alpha)\,,\\
\mathrm{d}c_{44} &= c^0_{44}(\mathrm{d}c^4-\sin(4\alpha)+\mathrm{d}s^4) + (c^0_{11}-2c^0_{12}+c^0_{22})\sin(2\alpha)/2\,,\\
\mathrm{d}c_{55} &= (-c^0_{55}+c^0_{44})\sin(2\alpha)\,,\\
\mathrm{d}c_{56} &= (c^0_{44}-c^0_{55})\cos(2\alpha)\,,\\
\mathrm{d}c_{66} &= (-c^0_{44}+c^0_{55})\sin(2\alpha)\,.
\end{aligned}
\tag{C.6}
$$

So that, again using Voigt notation,

$$\frac{\mathrm{d}[\mathbb{C}]}{\mathrm{d}\alpha} = \begin{bmatrix} \mathrm{d}c_{11} & \mathrm{d}c_{12} & \mathrm{d}c_{13} & \mathrm{d}c_{14} & 0 & 0 \\ \mathrm{d}c_{12} & \mathrm{d}c_{22} & \mathrm{d}c_{23} & \mathrm{d}c_{24} & 0 & 0 \\ \mathrm{d}c_{13} & \mathrm{d}c_{23} & 0 & \mathrm{d}c_{34} & 0 & 0 \\ \mathrm{d}c_{14} & \mathrm{d}c_{24} & \mathrm{d}c_{34} & \mathrm{d}c_{44} & 0 & 0 \\ 0 & 0 & 0 & 0 & \mathrm{d}c_{55} & \mathrm{d}c_{56} \\ 0 & 0 & 0 & 0 & \mathrm{d}c_{56} & \mathrm{d}c_{66} \end{bmatrix}. \tag{C.7}$$

D Material modeling error

The material model we use, like any material model, is an approximation of physical reality. Notably there is stiffness in all directions for any point in the body. However, if the adjacent toolpaths $\mathcal{C}_i^k$ and $\mathcal{C}_i^{k-1}$ on layer Ω_i do not abut one another, then the stiffness in that region will only be in the direction of the toolpaths $\mathcal{C}_i^k$ and $\mathcal{C}_i^{k-1}$, i.e., there will be no transverse stiffness. Nonetheless, we assume macroscopic stiffness in all directions due to the volume weighted approximation of Equation (24). And clearly our fabricated specimens would fail the validation process without this traverse stiffness. In reality, this traverse stiffness comes from the adjacent layers. To study this layer interaction effect and the accuracy of our material model, we perform the numerical homogenization of RVEs that include the adjacent layers. This is also an approximation as there is no periodic space filling unit cell in our optimized designs.

Figure D.1 shows the front and side sections of toolpaths corresponding to the layers Ω_{i-1}, Ω_i, and Ω_{i+1}, where the dashed lines indicate the RVE boundaries. The thickness and height of the toolpaths are $b = 0.6$mm and $h = 0.3$mm respectively. For convenience, the distance between the toolpaths is l for all three layers. Also, the toolpaths in Ω_i are orthogonal to the toolpaths in the adjacent layers. Thus, it can be shown that $l = b/\nu$ where ν is the volume fraction of the material in the RVE. For the layer Ω_i, the fibers are parallel to $\mathbf{e}_1$ which stiffness is $\mathbb{C}(0)$, cf. Equation (25). For layers Ω_{i-1} and Ω_{i+1} the stiffness is $\mathbb{C}(\pi/2)$ since the fibers are parallel to $\mathbf{e}_2$. For the numerical homogenization, we use fitted meshes for different volume fractions, cf. Figures D.3a, D.3b, and D.3c. We apply unit strains, impose periodic boundary conditions on the RVE, perform the finite element analyses, and evaluate the homogenized properties.

In order to validate our "effective" material model, we compute the homogenized properties using the RVE in dashed lines shown in Figure D.2 where each layer's stiffness is based on the volume fraction and the fiber orientation, cf. Equation (24). Thus, the stiffness for the material in Ω_i is $\nu\,\mathbb{C}(0)$, and for the adjacent layers Ω_{i-1} and Ω_{i+1} the stiffness is $\nu\,\mathbb{C}(\pi/2)$. For the numerical homogenization, we use the rectangular mesh shown in Figure D.3d.

Figure D.4 compares the homogenized properties of our effective material model versus the fitted mesh model for different volume fractions. We conjecture that, the homogenized stiffness of our effective model is higher than the fitted mesh model because the empty space between toolpaths carries load in the effective model but not in the fitted mesh model. Our future research will develop a more accurate material model.

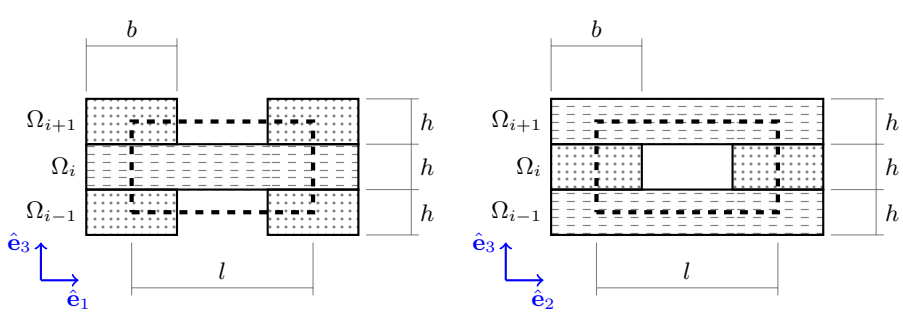

Figure D.1: RVE dimensions for fitted mesh.

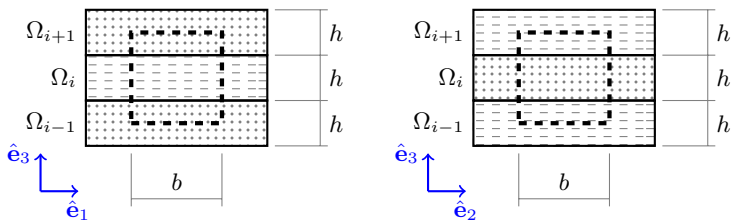

Figure D.2: RVE dimensions.

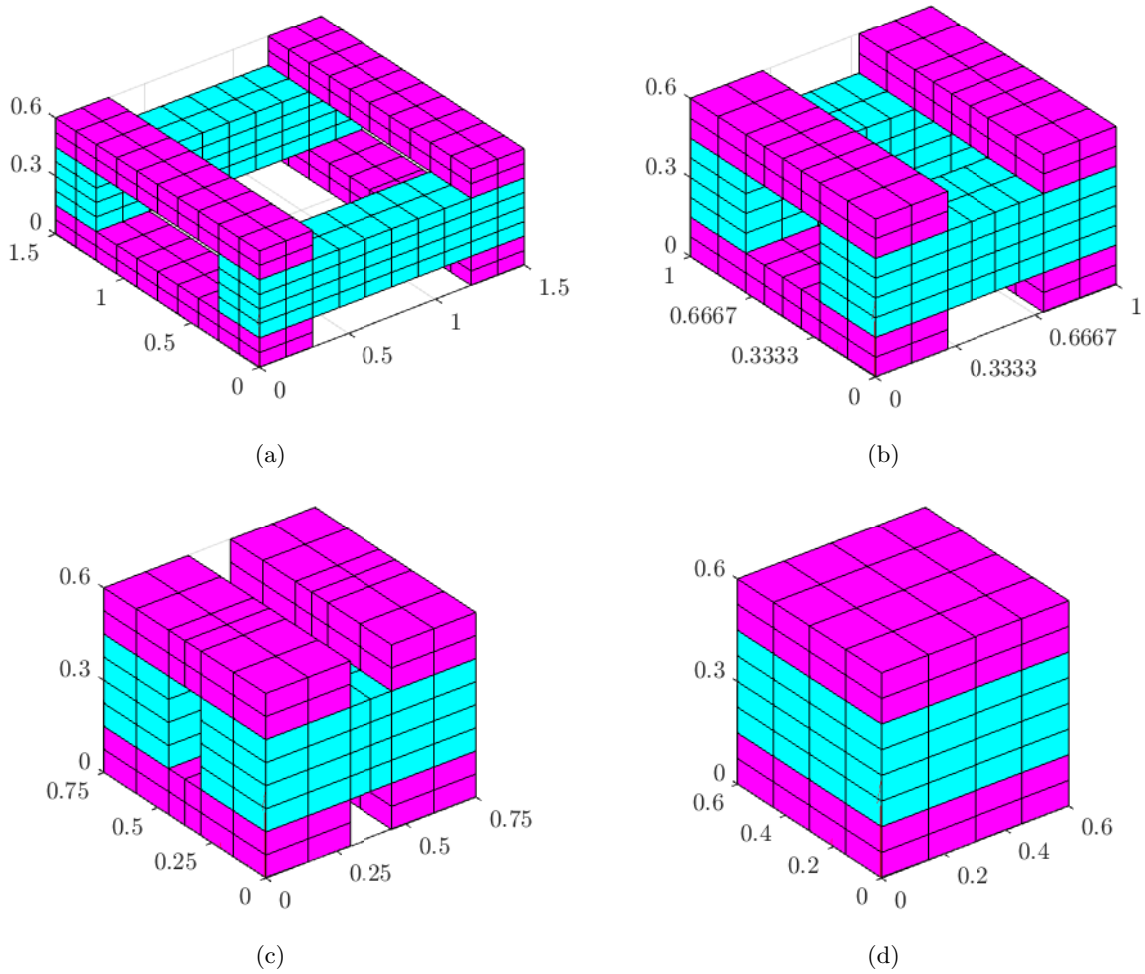

Figure D.3: RVE with adjacent layers using (a) a fitted mesh for $\nu = 0.4$, (b) $\nu = 0.6$, (c) $\nu = 0.8$, and (d) for our material model.

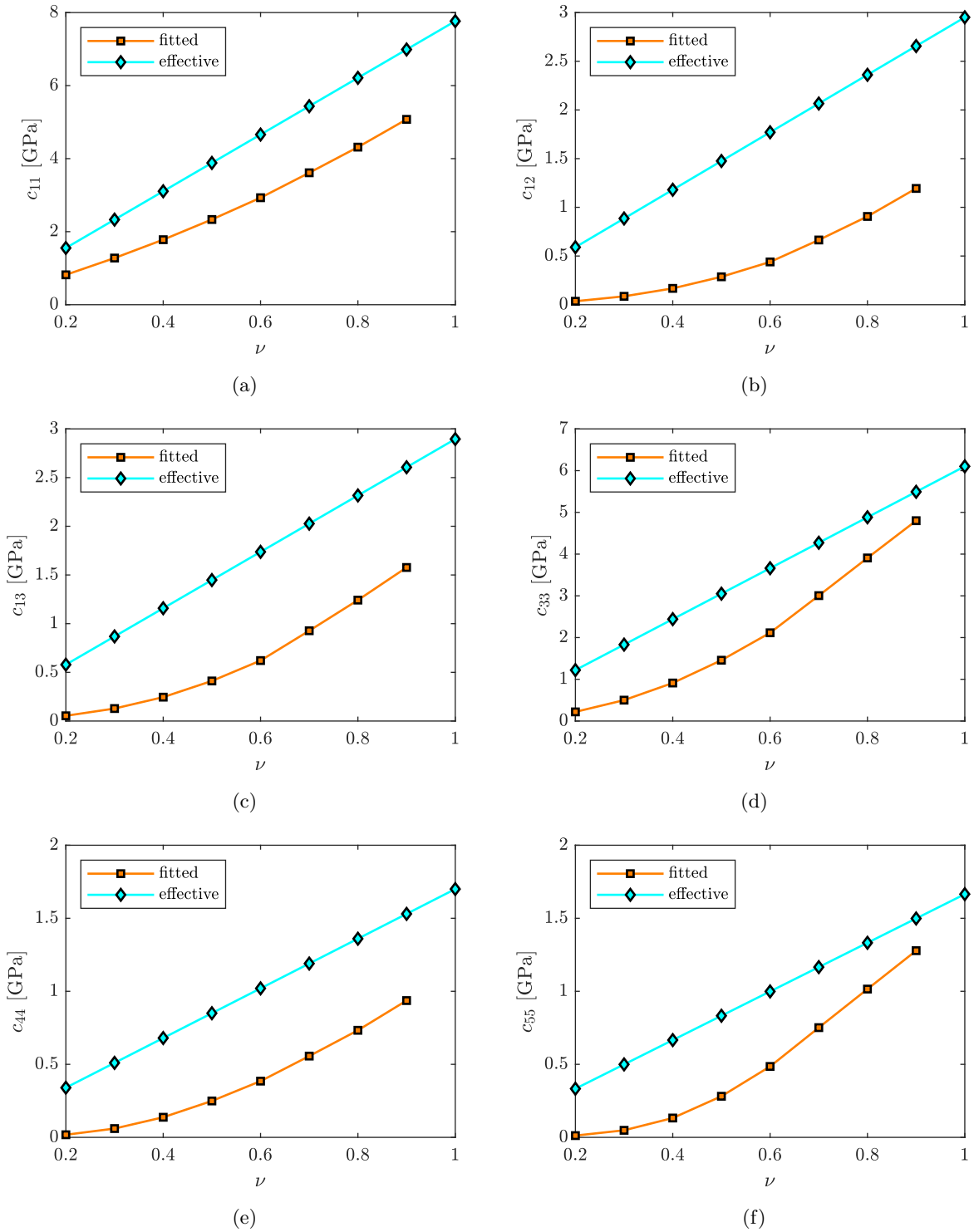

Figure D.4: Homogenized constitutive coefficients.